

## **Algorithm Technical Background Document**

### **MODIS FIRE PRODUCTS**

**(Version 2 .2 Nov. 10 1998)**

**(EOS ID# 2741)**

**Yoram Kaufman and Chris Justice**

**(MODIS Science Team)**

### **ABSTRACT**

The fire product is an interdisciplinary product shared between the MODIS Land and Atmosphere groups and designed to meet the needs of the global change research community. The product is in response to a growing demand for spatially explicit fire data to parameterize and validate various regional and global models. Fire is an important component of trace gas and particulate emission modelling, climate modelling, atmospheric transport and chemistry models, ecosystem dynamic models and models of land use change.

The MODIS fire products use the 1 km fire channels at 3.9 and 11  $\mu\text{m}$ . Fire observations will be made two times a day from the AM platform (10:30 am and pm) and four times a day when the PM platform (1:30 pm and 1:30 am) is also in orbit. As there is no on-board calibration for the high temperature sensors, the pre-launch calibration of the high gain channels will be augmented with post-launch vicarious calibration. The MODIS products build on heritage algorithms for operational fire monitoring used with the GOES and AVHRR sensors.

The MODIS fire products provide information on the location of a fire, its emitted energy, the flaming and smoldering ratio, and an estimate of area burned.

The fire products will be made available through EOSDIS as daily 1 km full resolution and spatially and temporally summarized products (10 km, 0.5 degree and 8 day and monthly), more suited for use by the modelling community. In addition, a collaboration has been formed with the University of Hawaii NASA-IDS project to develop a volcano and fire alert system in

near real time which is aimed initially at targetting high resolution data acquisitions but may prove to be of use to a broader environmental management community.

Pre-launch algorithm development, product simulation and prototyping are being undertaken using a suite of tools. Global 1 km AVHRR data are being used to explore the global data processing aspects of the product, simulation is being used to determine the sensitivity and accuracy of the algorithms, laboratory measurements are being used to understand the physics of fire characterization, and MODIS Airborne Simulator are being used to test the spectral and spatial aspects of the algorithm. Post launch validation will use high resolution data, regional aircraft campaigns and ground data collection.

In the post-launch period it is intended to combine the diurnal sampling of the MODIS fire data with high temporal frequency geostationary data and high spatial resolution for Landsat 7 and ASTER to provide a comprehensive fire monitoring system.

## **Contents**

### **1.0 Introduction**

### **2.0 Overview and Technical Background**

#### **2.1 Science Rationale**

#### **2.2 Current Fire Detection Procedures**

##### **2.2.1 GOES satellite and fire analysis**

##### **2.2.2 Defense Mapping Satellite Program (DMSP) fire detection**

##### **2.2.3 Landsat fire detection**

##### **2.2.4 Airborne fire monitoring**

##### **2.2.5 AVHRR fire detection**

###### **2.2.5.1 The AVHRR and active fire studies**

###### **2.2.5.2 AVHRR fire detection techniques**

#### **2.3 MODIS Instrument Characteristics Associated With The Fire Products**

##### **2.3.1 MODIS Simulation Studies**

###### **2.3.1.1 Landsat observations of the 1988 Yellowstone Fire**

###### **2.3.1.2 MODIS Airborne Simulator data: SCAR-C experiment**

###### **2.3.1.3 AVHRR prototyping of MODIS global active fire products**

#### **2.4 The Intended MODIS Fire Product User Community**

#### **2.5 An Example of the Use of Satellite Derived Fire Characteristics**

### **3.0 MODIS Algorithm Description**

#### **3.1 Theoretical description**

##### **3.1.1 Physics of the problem**

##### **3.1.2 Description of algorithm**

##### **3.1.3 Variance of uncertainty estimates**

#### **3.2 Practical Considerations**

##### **3.2.1 Programming/procedural considerations**

##### **3.2.2 Calibration and validation**

##### **3.2.3 Quality control and diagnostics**

##### **3.2.4 Exception handling**

3.2.6 Data dependencies

3.2.7 Output product

3.3 Constraints, limitations, and assumptions

#### **4.0 An outline of the agenda for product research and development**

4.1 Prelaunch Research

4.2 Postlaunch Research

#### **Acknowledgments**

#### **List of Figures**

#### **References**

#### **Appendix 1. Previous ATBD Reviews and Response**

## 1.0 INTRODUCTION

The MODIS fire products build and improve on the experience of fire assessment primarily using the NOAA-AVHRR and GOES systems. Currently no one sensing system provides the instrument characteristics needed for an effective global fire monitoring program. The MODIS sensor has been designed to include characteristics specifically for fire detection and will provide a unique capability over existing sensors in terms of fire monitoring. The fire products will include an identification of the occurrence of thermal anomalies, an estimate the total emitted energy from the fire, and ratio of smoldering to flaming components. The products will be available at full resolution and as spatial summaries and temporal composites. Daytime and nighttime fire distributions products will be identified. The fire products will be developed on the basis of convergence of evidence from different spectral information.

Many users are ultimately interested in the area of land that is burned. This can be obtained through detection of burn scars. MODIS will offer unique spatial and radiometric capabilities for burn scar detection. Automatic procedures for burn scar detection are under development using the AVHRR which incorporate the identification of fire occurrence as one piece of information in a hybrid multitemporal approach to scar detection and area estimation. Automated globally applicable procedures for direct measurement of area burned will be ready for implementation in the post-launch period.

## 2.0 OVERVIEW AND TECHNICAL BACKGROUND

### 2.1 SCIENCE RATIONALE

The MODIS fire products will provide an important input to research programs in several in different scientific disciplines. Fire is an important process within a significant number of terrestrial biomes, and the release of gases and particulate matter during biomass burning is an important contributor to the chemical reactions and physical processes taking place in the atmosphere. Fire is a significant and continuous factor in the ecology of savannas, boreal forests and tundra, and plays a central role in deforestation in tropical and sub-tropical regions. In addition, on a periodic basis, extensive fire occurs in many temperate biomes such as forests, grasslands, and chaparral.

Monitoring the location and aerial extent of biomass burning and its associated effects are important in the context of the goals and objectives of the US Global Change Research Program.

- Fire changes the physical state of the vegetation, releasing a variety of greenhouse gases into the atmosphere. There is presently great uncertainty as to the magnitude of the sources and sinks of these greenhouse gases. For example, the net annual release of carbon into the atmosphere due to the clearing and conversion of tropical forests for agricultural purposes (where biomass burning is a key tool used in the conversion process) is thought to contribute approximately 30% to the net annual increase in the concentration of atmospheric CO<sub>2</sub>. In addition, there is an interest in changes in

regional fire regimes under different climate change scenarios. For example, arguments have been made that an increase in average air temperature in northern latitudes will lead to a decrease in the natural fire return interval and an increase in fire severity in boreal forest and tundra ecosystems. This in turn, could lead to a significant reduction of the carbon stored in these ecosystems, with a comparable increase in atmospheric carbon.

- The release of chemically-reactive gases during biomass burning strongly influences chemical processes within the troposphere. In tropical regions, biomass burning has been shown to strongly influence regional and global distributions of tropospheric ozone and has been related to acid deposition. Studies have shown that intensive biomass burning associated with naturally occurring forest fires, deforestation practices and savanna management is a major source of trace gases such as NO, CO<sub>2</sub>, CO, O<sub>3</sub>, NO<sub>x</sub>, N<sub>2</sub>O, NH<sub>3</sub>, SO<sub>x</sub>, CH<sub>4</sub>, other non-methane hydrocarbons, as well as an abundant source of aerosols (Stith et al., 1981; Crutzen et al., 1985; Fishman et al., 1986; Andreae et al., 1988; Browell et al., 1988; Kaufman et al., 1992).

Preliminary global estimates indicate that annual biomass burning may be associated with 38% of the ozone in the troposphere; 32% of global carbon monoxide; more than 20% of the world's hydrogen, nonmethane hydrocarbons, methyl chloride and oxides of nitrogen; and approximately 39% of the particulate organic carbon (Levine, 1991; Andreae, 1991). Although these estimates include a wide range of uncertainty, it is becoming evident that these emissions may be as important to global atmospheric chemistry as industrial activities in the developed world (Crutzen et al., 1985; Crutzen and Andreae, 1990). It is estimated that as much as 70 to 80% of the total biomass burned globally each year is burned in the equatorial and subtropical regions (Greenburg et al., 1984; Andreae, 1991). Some of the most intensive biomass burning activities are associated with deforestation and grassland management in South America, South East Asia and sub-Saharan Africa (Malingreau, 1990). The tropics receive the maximum amount of visible and ultra-violet radiation, thus acting as a primary driving force for atmospheric circulation. Since most biomass burning in the tropics is limited to a burning season, the temporal and spatial concentration of emissions are expected to have a noticeable impact on atmospheric chemistry and climate in the tropics and globally as a result of increased trace gas emissions and the direct and indirect radiative effects of smoke aerosols.

- The release of soot and other particulate matter during fires leads to significant physical changes within the troposphere in the region down-wind from the fire. First, depending on the single scattering albedo, particulate matter can result in a warming or cooling of the climate. Second, particles emitted from fires can effect cloud microphysics and radiative properties. The particles serve as cloud condensation nuclei and result in an increase in cloud cover and more reflective clouds. This increase in cloud cover increases the albedo of the atmosphere and reduces the average air temperature. In addition, these clouds also affect precipitation patterns.

Recent analyses have indicated that the direct and indirect radiative effects of aerosols from biomass burning may be significant to the radiative balance of the earth and may be a major factor in climate change (Coakley et al., 1983; Twomey et al., 1984; Charlson

et al., 1991; Kaufman et al., 1991; Twomey, 1991; Penner et al., 1992). Although the overall effects of aerosol loading from biomass burning are not very well understood. The two primary radiatively active components of aerosol emissions from biomass burning are particulate organic and graphitic carbon. Particulate organic carbon is the largest constituent and generally serves to scatter incoming solar radiation, while graphitic carbon particles can increase the solar radiation absorption in the atmosphere and clouds. The primary direct effect of particulate organic carbon aerosols is that they reflect incoming solar radiation back to space and act to cool the surface. The indirect effects of particulate organic carbon are associated with the ability for these aerosols to act as cloud condensation nuclei (CCN). Clouds are one of the most important controls on the heat balance of the earth.

A number of studies have been done to characterize the effects of aerosols due to anthropogenic pollution and biomass burning on clouds and climate (Stith et al., 1981; Twomey et al., 1984; Coakley et al., 1987; Hallett et al., 1989; Hudson, 1991; Rogers et al., 1991; Leitch, et al., 1992). For thin to moderate clouds, increased CCN loading is thought to result in an increase in reflectivity and cloud albedo. Increased CCN loading generally results in increased droplet formation of a smaller size given a constant amount of available water. Clouds which are made of smaller droplets are usually assumed to be whiter, reflect more solar radiation and may be less likely to produce rain (Radke et al., 1990; Andreae, 1991). Recent results obtained by Kaufman and Nakajima (1993), which focused mainly on low level cumulus and stratocumulus clouds, indicated that in the Amazon high concentrations of smoke aerosols lead to a decrease in the cloud drop size but actually reduced the reflectivity of related clouds as a result of absorption by graphitic carbon. These results are in line with those presented by Twomey (1977) which suggested that for optically thin clouds an increase in cloud drop concentration would result in a greater reflectivity, while for clouds which are optically thick and very bright to begin with, the effect of increased cloud drops would be dominated by absorption and reduction of cloud brightness.

- The results of natural fire or processes associated with fire affect the exchange of energy and water between land surfaces and the atmosphere. Fires can result in a decrease in the surface albedo and increase in the amount of solar radiation reaching the soil layer at local and regional scales. These, in turn, increase the amount of absorbed energy from incoming solar radiation, and generally increase the ground temperature. The changes in ground temperature affect a wide range of processes, including nutrient and water availability and microbial respiration. Removal of the plant canopy during fire reduces the amount of evapotranspiration and typically results in more water runoff. In tropical forests, the land clearing associated with biomass burning has resulted in a significant reduction of total precipitation in the region, and increase the surface runoff, soil erosion and river sedimentation. In tropical forests, activities associated with biomass burning and land clearing lead to an overall reduction in the amounts of precipitation in regions down-wind from the affected areas. First, the smoke from fires act as cloud condensation nuclei, and form additional water droplets in clouds; however, these droplets are typically smaller than those found in clouds found over tropical regions, and result in lower levels of precipitation. Second, land clearing and continuous burning leads to the conversion of forest to savanna. The

grasses dominating the savannas have a much lower rate of evapotranspiration than trees, resulting in less water being returned to the atmosphere. Finally, savannas are much more susceptible to surface runoff, resulting in more precipitation flowing into streams and rivers. In addition, once the overlying vegetation of a tropical forest has been removed the exposed soil surface then becomes susceptible to erosion and the wetland and river systems are subject to sedimentation.

In boreal forests, there is a dependence on the melting and formation of permafrost and the occurrence of fire, which in turn has a strong influence on the hydrology of these sites. In boreal forests, fire effects the flow of energy between the atmosphere and ground layer dramatically. First, fire removes a large portion of the vegetation layer which shades the ground, thus increasing the solar energy reaching the ground. Second, it decreases the albedo of the ground layer, increasing the amount of energy absorbed by the ground layer. And third, fire removes much of the dead organic matter layer which insulates the ground. It has been shown that during the first year after a fire in a black spruce forest underlain by permafrost, there is a 5 K to 7 K increase in the temperature of the ground layer, which in turn causes a melting of the permafrost layer and an increase in the soil moisture in the active layer. The ground layer of these fire-affected areas remains affected for at least 15 to 25 years, with the depth of thaw of the active layer increasing also. Because of the melting permafrost and lack of a transpiring vegetation layer, during the initial years after a fire there is an increase in the moisture of the ground layer; however, after a few years, when the active layer becomes deeper, there is better drainage for the surface moisture, which then decreases. Finally, after about 20 to 25 years, the ground layer becomes cooler (as the vegetation layer becomes re-established, along with an increase in the depth of the dead organic matter layer), the active layer becomes shallower, and the ground layer moisture increases because of poorer drainage.

- Fires have several direct and indirect effects on terrestrial ecosystems. First, the pattern of fire (which includes its spatial distribution, fire return interval and severity of burning ) directly controls plant community development on those landscapes where biomass burning occurs. Fire favors those plants and tree species which have developed adaptations to fire (e.g., vegetative reproduction and fire-resistant seeds and cones) and eliminates those species which are less resistant to fire. Second, fire indirectly affects plant community development in a variety of ways, including (a) addition of key plant nutrients through ash fertilization or increased soil decomposition; (b) depletion of key plant nutrients through surface runoff or increased soil leaching; and (c) altering soil temperature and moisture. Finally, chemical reactions of the gases released by fire leads to an increase in atmospheric ozone and the deposition of acidic compounds downwind from fires, which in turn can effect the physiology of plants and ecosystems in these areas.

## 2.2 CURRENT FIRE DETECTION PROCEDURES

### 2.3.1 GOES satellite and fire analysis

Recent work has shown the potential of meteorological geostationary satellites to monitor biomass burning activities. The Visible Infrared Spin Scan Radiometer and Atmospheric Sounder (VAS) available on the GOES satellite can be used to locate active fires by utilizing the visible, shortwave infrared (IR) (4 $\mu$ m), and longwave IR (11  $\mu$ m) window data. Since 1980 the GOES VAS instrument on GOES-4 and all successive GOES satellites have provided multispectral monitoring of North and South America in the visible and 12 infrared spectral bands between 4 and 15  $\mu$ m (See Table 1).

**Table 1. GOES Satellite Spectral Channels**

GOES Location:      GOES-East at 75° W,      GOES-West at 135° W			
Channel	Wavelength* ( $\mu$ m)	Spectral Band	Spatial Resolution (km)
Visible	0.55 - 0.75	Visible	0.9
1	14.6 - 14.8	CO <sub>2</sub>	13.8
2	14.3 - 14.7	CO <sub>2</sub>	13.8
3	14.1 - 14.4	CO <sub>2</sub>	6.9 or 13.8
4	13.8 - 14.2	CO <sub>2</sub>	6.9 or 13.8
5	13.2 - 13.5	CO <sub>2</sub>	6.9 or 13.8
6	4.5 - 4.6	CO <sub>2</sub>	13.8
7	12.5 - 12.8	CO <sub>2</sub>	6.9 or 13.8
8	10.4 - 12.1	Window	6.9 or 13.8
9	7.2 - 7.4	H <sub>2</sub> O	6.9 or 13.8
10	6.4 - 7.1	H <sub>2</sub> O	6.9 or 13.8
11	4.4 - 4.5	N <sub>2</sub> O	13.8
12	3.8 - 4.1	Window	13.8

\* GOES-7

From its vantage point approximately 36,000 km above the equator, the VAS radiometer is capable of sensing both visible and upwelling radiation in two window channels, three water vapor channels and seven spectral regions within the CO<sub>2</sub> and N<sub>2</sub>O bands. The spatial resolution is 0.9 km in the visible region and 6.9 or 13.8 km instantaneous geometrical fields of view (IGFOV) at nadir in the infrared, depending on the detectors being used. All of the infrared bands are available at 13.8 km and the seven longwave channels are also available at 6.9 km resolution. In the multispectral imaging (MSI) mode four spectral channels can be observed every half hour: the visible at .9 km, the 11  $\mu$ m window at 6.9 km, and two other infrared channels at 13.8 km resolution. Since the infrared detectors are sampled every 8  $\mu$ s (during which the footprint travels 0.084 mr), the large detector IGFOVs are oversampled by a factor of 4.6 and the small detectors are oversampled by a factor of 2.3 (Montgomery and Endres, 1985). This results in sampled resolution of 3.0 km east/west by 6.9 km north/south at



subpoint for the small detectors and 3.0 km east/west by 13.8 km north/south for the large detector.

The GOES VAS longwave and shortwave infrared window channels 8 (11  $\mu\text{m}$ ) and 12 (4  $\mu\text{m}$ ) are often used to determine surface temperatures. During daylight hours channel 12 is affected by reflected sunlight, but it does offer the advantage of being less attenuated by water vapor than channel 8. Typically the difference in brightness temperatures between channels 8 and 12 is due to reflected solar radiation, surface emissivity differences, and water vapor attenuation. This normally results in brightness temperature differences of 2-5 K. Larger differences occur when one part of a pixel is substantially warmer than the rest. The hotter portion will contribute more of the radiance observed in the shorter wavelengths than in the longer wavelengths. As the temperature increases the peak of the Planck function shifts toward shorter wavelengths, which results in the radiant contribution increasing more rapidly in channel 12 than channel 8 for higher temperatures. This characteristic makes it possible to estimate both the target temperature ( $T_t$ ) and size ( $p$ ) of the subpixel area of fire by considering the upwelling thermal radiance values obtained by both channels in a pair of nonlinear equations (Dozier, 1981; Matson and Dozier, 1981).

The technique of Matson and Dozier (1981) was adapted to GOES VAS data to monitor biomass burning in selected regions of South America in 1983 and 1988 (Prins, 1989). The fires were identified in the GOES VAS imagery by manually locating hot spots in the 4  $\mu\text{m}$  channel and verifying the presence of fire by the presence of a smoke plume in the visible imagery. Furthermore, to be designated as a fire pixel, the pixel must exhibit elevated brightness temperature values in both the 4 and 11  $\mu\text{m}$  channels. Although, the spatial resolution of GOES VAS data (7km/14km) is a limiting factor in detecting fires, comparisons with AVHRR data indicated that the decreased spatial resolution does not severely hinder the ability of the VAS instrument to detect subpixel fires, except in cases of isolated fires. Typically the area covered by a VAS field of view (FOV) includes a number of fires which act collectively to indicate the presence of fire(s). In addition, in some cases the lack of horizontal resolution of the VAS serves as an advantage in that the sensor rarely saturates for large or hotter fires (Menzel et al., 1991; Prins and Menzel, 1992).

The high temporal resolution of GOES VAS data provides unique opportunities to monitor aspects of biomass burning which are not readily obtained with other systems. Sequences of half-hourly visible data can be used to verify that the hot spots sensed in the IR are actually related to fires. Diurnal GOES visible and IR data are extremely useful in determining the diurnal variations in fire activity and the transport of related aerosols.

In order to identify fire activity in GOES VAS imagery operationally, it is necessary to automate the process. The automated algorithm must be capable of distinguishing pixels which contain fire activity and provide estimates of the size of the fires. One such algorithm is the GOES VAS Automated Biomass Burning Algorithm (ABBA) recently developed at the Cooperative Institute for Meteorological Satellite Studies (CIMSS) (Prins and Menzel, 1993). The algorithm was developed using the results obtained during the 1983 and 1988 burning seasons in South America. The determination of subpixel fire activity is based on modifications of the Matson and

Dozier (1981) technique applied to GOES VAS IR data described in the following paragraphs.

When the GOES VAS radiometer senses radiance from a field of view (FOV) containing a target(s) of blackbody temperature  $T_t$  occupying a portion,  $f$ , (between zero and one) of the FOV and a background of blackbody temperature  $T_b$  occupying the remainder of the FOV,  $(1-f)$ , the following equations represent the radiance sensed by the instrument at 4 and 11  $\mu\text{m}$ , respectively

$$L_4(T_4) = f L_4(T_t) + (1 - f) L_4(T_b) + (1 - \epsilon_4) L_{4, \text{solar}}$$

$$L_{11}(T_{11}) = f L_{11}(T_t) + (1 - f) L_{11}(T_b)$$

where :

$$L = B_s + \int_{p_s}^0 B \frac{d\epsilon(p)}{dp} dp$$

and

$L$	integrated upwelling thermal radiance at the top of the atmosphere wavelength
$\epsilon$	emissivity of the surface
$L_{4 \text{ solar}}$	solar radiance at earth surface
$\epsilon_s$	transmittance to the top of the atmosphere
$B(p)$	Planck function of the air at altitude with pressure $p$
$B_s$	Planck function for the surface temperature
$T$	observed brightness temperature
$p_s$	indicates pressure at the surface
$p$	transmittance at different pressure levels ( $p$ )

If  $T_b$ ,  $T_4$ , and  $T_{11}$  are known these two equations can be solved for  $T_t$  and  $p$  using numerical iteration techniques. The GOES VAS ABBA only processes those pixels which pass certain thresholds.

In order to distinguish fire pixels from non-fire pixels and to obtain realistic estimates of subpixel fire activity, it is important to get an accurate representation of the background temperature (within 1 K) for the region being considered. Since surface temperature observations are not routinely available in the study areas, it is necessary to obtain these values from the satellite data. The average 4 and 11  $\mu\text{m}$  background brightness temperatures and standard deviations obtained from satellite data within a given subsection of the area being studied can be used to identify fire pixels especially in areas where the surface characteristics are not homogeneous. The algorithm obtains the 4 and 11  $\mu\text{m}$  brightness temperature values and calculates 4 and 11  $\mu\text{m}$  average background temperatures for 150 km by 150 km subsections within the study area using thresholding techniques to eliminate those pixels which contain clouds. The

average background temperature is calculated using only those pixels where the 4  $\mu\text{m}$  brightness temperature is less than 315 K, the 11  $\mu\text{m}$  brightness temperature is greater than 285 K, and the difference between the 4 and 11  $\mu\text{m}$  brightness temperatures is greater than -4 K and less than 7 K (these thresholds are based on climatological data for the region). In some cases it is not possible to determine a background temperature for a given subsection due to cloud contamination. In these cases an iterative approach is used to interpolate between adjacent sections which are not cloud contaminated.

Next the algorithm scans the data and eliminates those pixels which do not contain fires utilizing a series of thresholding tests. Test 1 makes use of the different brightness temperatures in the 4 and 11  $\mu\text{m}$  channels, which is typically 2-5 K due to reflected solar radiation, surface emissivity differences and water vapor attenuation. If the difference between the observed brightness temperature in the 4 and 11  $\mu\text{m}$  channels is less than or equal to the difference between background values for that subsection, the pixel is disregarded. Test 2 looks at the difference between the observed and background 4  $\mu\text{m}$  brightness temperatures taking into consideration the heterogeneity of the subsection containing the pixel. If the difference is less than 1.5 times the standard deviation of the 4  $\mu\text{m}$  background temperature or a minimum of 2 K, the pixel is disregarded. In applications of the algorithm these two tests eliminate approximately 90% of the non-fire pixels.

The observed and background brightness temperature values for those pixels which pass tests 1 and 2 are corrected for transmissivity, emissivity, and solar reflectivity (4  $\mu\text{m}$  brightness temperature only). The algorithm first applies the transmissivity corrections. It is difficult to adequately define corrections for cloud, haze, and water vapor attenuation. It is assumed that there is little variation in the amount of total water vapor in the atmosphere within a given region. For South America, the surface emittance and atmospheric contribution were determined for total precipitable water amounts of 20, 25, and 30 mm, which are typical for the Cerrado, mixed and selva regions, respectively. These transmissivity corrections were applied to the observed values based on which vegetation type the pixel was located in. The attenuation due to the smoke and clouds that form directly over the fire is important to consider, but it is difficult to determine. In earlier work (Prins 1989), a crude estimate of the transmissivity correction directly over the fire was determined by considering the effect of plumes on the background brightness temperature in both window channels downwind of approximately 50 fires and then extrapolating to the offset for a fire covered by a plume with an average visible brightness count of 115. The corrections were 2 and 4 K in the 4 and 11  $\mu\text{m}$  channels, respectively. This average brightness value was found to be valid after considering over 1600 additional fires in 1988, 1989 and 1991 with a mean brightness value of 116 counts and standard deviation of 20 counts. Inspecting non-fire cloud situations confirmed that a 2 and 4 K offset is probably valid for fire pixels with corresponding maximum visible brightness values ranging from 80 to 150 counts. These offsets are applied to all pixels which pass tests 1 and 2.

Surface emissivity correction is accomplished with a lookup table which assigns a surface emissivity value for a given pixel based on its location. The lookup table contains 4 and 11  $\mu\text{m}$  emissivity values for 2° by 2° sections within the study area representing 3 vegetation types: selva, Cerrado, and mixed, suggested in a 1980 surface vegetation map of South America published by UNESCO as well as by radar data. The

corresponding emissivities for the selva, mixed, and Cerrado regions are 0.96, 0.90, and 0.87 in the 4  $\mu\text{m}$  region and 0.97, 0.92, and 0.90 in the 11  $\mu\text{m}$  region, respectively. The 11  $\mu\text{m}$  observed and background temperatures are adjusted for surface emissivity. The adjusted 11  $\mu\text{m}$  background temperature is then used to determine the solar reflectivity radiance offset for the 4  $\mu\text{m}$  background brightness temperature. The 4  $\mu\text{m}$  observed brightness temperature is subsequently adjusted for solar reflectivity contamination as well as emissivity.

The adjusted values are tested further to eliminate any remaining non-fire pixels. Test 3 requires that the 4  $\mu\text{m}$  corrected observed temperature must be greater than 300 K and the 11  $\mu\text{m}$  corrected observed temperature must be greater than 295 K. Test 4 eliminates all pixels where the difference between the corrected 11  $\mu\text{m}$  observed and background temperatures is less than 1 K. Test 5 eliminates all pixels where the difference between the corrected 4  $\mu\text{m}$  observed and background temperatures is less than 5 K. All pixels which pass Tests 1 through 5 are processed to determine the view angle corrected subpixel area on fire and the average target temperature of the area on fire. Finally, test 6 disregards pixels with fire target temperatures less than 400 K in an attempt to eliminate recently burned areas which appear hot in relation to the background temperature.

Although algorithm verification with ground truth data for individual fires is not complete, the GOES values appear to be similar to those cited by others (Molion, 1991; Setzer and Pereira, 1991a). A visual comparison with AVHRR images in 1988 and 1989 indicates that the GOES VAS algorithm correctly located the major burning areas. Results obtained using the GOES VAS ABBA indicate that the lower bound of resolvable fires with this algorithm is about 0.1 km<sup>2</sup>. This implies that GOES VAS data miss the smaller isolated fires. In regions of intense burning, the area covered by a single VAS FOV includes a number of fires which act collectively to produce an average temperature and total area burned. An attempt was made to characterize the errors associated with the GOES VAS manual technique (Prins and Menzel, 1992). The largest uncertainty lies in the sensitivity of the algorithm to corrections for cloud and haze contamination and can result in a relative error of 33% if the correction is off by 1K.

The utility of diurnal GOES VAS data is not in the ability to provide precise values of the location or aerial extent of fire activity, but in the opportunity to determine the diurnal distribution of fires in different biomes. Diurnal GOES VAS infrared images for South America indicated that the optimum time to monitor biomass burning is around 1530 UTC (12:30 local time). Biomass burning estimates determined from GOES satellite measurements 3-6 hours later are a factor of 2 to 20 times less (Menzel et al., 1991; Prins and Menzel, 1992).

## 2.2.2 Defense Mapping Satellite Program (DMSP) fire detection

The orbital characteristics of the DMSP satellite are very similar to the NOAA satellites (Table 2). It is in a polar sunsynchronous orbit, with an equatorial crossing time of 10:50 and 22:50 local solar time. The unique characteristic of the DMSP platform is the low-light visible sensor which is operated routinely at night. The sensitivity (gain) of the instrument can be adjusted to provide "day-like" visible imagery on

moonlit nights. Even though the instrument was designed for meteorological purposes, the visible-light instrument is sensitive to other terrestrial light sources, such as city lights, gas flares, auroras, lightning, and fires (Croft, 1978; Sullivan, 1989). This imagery has been demonstrated to be a useful tool for monitoring fire activity at night, particularly in remote regions where there are few city lights (e.g., African savannas) (Cahoon, et al., 1992b). Historically, the DMSP archive was primarily in photographic form. The instrument has an adjustable gain and the archived data does not include instrument calibration information making any quantitative comparison between light sources impossible. Digital data and improved access to data from this system are have recently been developed by NOAA NGDC (C. Elvidge- personal communication). As far as the authors understand, there is no systematic production of regional fire data sets from the DMSP.

**Table 2. Sensor Characteristics:**

Visible:	0.4 - 1.1 $\mu\text{m}$ (half power response points: 0.57 and .97 $\mu\text{m}$ )
IR	8-13 $\mu\text{m}$
Total Swath Width:	3000 km
Ground Resolution:	2.7 km Global coverage 0.6 km Limited coverage
IFOV:	Normal Mode: 5.33 milliradians High Res. Mode: 0.766 milliradians

---

### 2.2.3 Landsat fire detection

The high spatial resolution sensor of the Landsat Thematic Mapper (TM) includes a middle infrared channel (2.08-2.35  $\mu\text{m}$ ) with a 30 m spatial resolution, which permits active fires to be detected. A 700 K fire that occupies 20% of the 30 m pixel will saturate the middle infrared TM channel. A recent study using the TM 1.6  $\mu\text{m}$  channel has also provided some interesting preliminary results, estimating fire intensity through interpretation of the spectral response from the resulting ash layer (Riggan et al 1993). With the advent of increased access to Thematic Mapper data from Landsat 7 it is hoped that MODIS, Landsat 7 and ASTER will provide a useful multiscale sampling of fire activity.

### 2.2.4 Airborne Fire Monitoring

Various multispectral airborne sensors have been developed and used for vegetation monitoring. Few have been designed with the purpose of fire monitoring. One such Fire Imaging Spectrometer system has been developed at NASA Ames Research Center (Riggan et al 1993). The spectrometer incorporates the chassis and the

optics of a Texas Instruments RS-25 thermal line scanner. It is a four-channel 14 bit digital system with detectors of silicon, indium- gallium arsenide, indium antimonide and mercury cadmium telluride. The initial configuration for the instrument was to have spectral channels with wavelengths at 0.58-0.7, 1.55-1.75, 3.96-4.05, and 10-12 microns. Spatial resolution is 2.5 m for every 1000 m aboveground. The three infrared channels were calibrated in the laboratory to temperatures as high as 900 K.

This system has been used to provide unsaturated high spatial resolution data over high-intensity fires. Data were reported for two fires in Brazil showing fire characteristics (ibid). Temperatures for savanna fires fell within the range 933-1336 K. The soil surface radiated little energy after the passage of the flaming front. Radiances at 1.65  $\mu\text{m}$  in cooled ash and unburned ground were 1-2% of those observed in the flaming zone. Fires in felled forest involved a wide area of residual combustion following the passage of the fire. Temperatures ranged from 846 - 1117 K and flaming activity was less homogeneous than in the savanna fire. In general, fires in the smoldering state range from 500-600 K (Ward - personal communication).

Such airborne sensors provide the best opportunity for detailed characterization of fires and would provide a useful means to calibrate and validate the ability of satellite systems to detect and quantify fires. Airborne sensors provide the means to measure both fire size and temperature and to characterize the spatial pattern of fire distribution and evolution of a given fire event.

The MODIS Airborne Simulator (MAS) is providing the basis for further development of the pre-launch fire algorithms and validation of the MODIS fire products (see Section 3.2.2.2). The MAS is a modified Daedalus Wildfire scanning spectrometer which flies on the NASA ER-2. A description of the heritage of the instrument is provided in the Earth Observer (Nov./Dec. 1992). The MAS is currently a 50 band instrument. Since January 1995 the MAS has a 50 channel digitizer which records all 50 bands at 12 bit resolution. The MAS has been flown on two missions specifically for the purpose of MODIS fire simulation (SCAR C and SCAR B). Details of these missions and the available data can be found at <http://ltpwww.gsfc.nasa.gov/MODIS/MAS>. The MAS scanner sub assembly collects image data with an IFOV of 2.5 mrad, giving the data a 50 m IFOV from a 20 km altitude. The scan width at this altitude is approximately 37 km.

## 2.2.5 AVHRR Fire Detection

### 2.2.5.1 The AVHRR and active fire studies

The current sequence of NOAA (National Oceanic and Atmospheric Administration) satellites has been in continuous operation since Oct. 1978.

The AVHRR is a scanning radiometer measuring reflected and emitted radiation in four channels on board the satellites NOAA-6, - 8, -10, and -12. and in five channels on board NOAA-7, - 9, -11 -13, and -14 (Table 3). The term "very high resolution" refers to a high radiometric resolution. AVHRR data are recorded to 10 bit precision. For the thermal infrared channels, on-board calibration exists through the regular measurement of the deep space and a blackbody of known temperature on board. No inflight

calibration exists for the visible and infrared channels. However, since these channels are widely used for vegetation monitoring, efforts have been made to monitor the calibration through the repeated measurement of surface targets which are assumed to be stable. Daily global coverage is achieved at the expense of the wide scan angle of the sensor (which reaches a maximum of  $55.4^\circ$  on either side of the nadir) and the large instantaneous field of view (IFOV). This viewing geometry gives rise to a coarse 1.1 km ground resolution for pixels at nadir. The wide scan angle leads to pixels at image edges being over three times the size of pixels at nadir. A detailed description of the platform and sensor characteristics of the entire TIROS-N family are provided by Kidwell (1991) and Schwalb (1982).

**Table 3 Characteristics of NOAA-AVHRR Systems****NOAA satellites and periods of operation:**

TIROS-N	19.10.1978 - 30.01.1980	(NASA funded prototype)
NOAA-6	27.06.1979 - 05.03.1983	
	03.07.1984 - 16.11.1986	
NOAA-7	19.08.1981 - 07.06.1986	
NOAA-8	20.06.1983 - 12.06.1984	
	01.07.1985 - 31.10.1985	
NOAA-9	25.02.1985 - 07.11.1988	
NOAA-10	17.11.1986 - 17.09.1991	
NOAA-11	08.11.1988 - present	
NOAA-12	17.09.1991 - present	
NOAA-14	xx.xx.xxx - present	

**Orbital Parameters:**

Orbital Type:	sun synchronous, near polar	
Orbital Inclination:	98.8°	
Nominal Altitude:	833 - 870 km	
Orbital Period:	102 min	
Orbits/Day:	14.2	
Orbit Repeat cycle:	9 days	
Equatorial Crossing	Descending	Ascending
Times <sup>a</sup> (at launch)	02:30h	14:30h (NOAA-7, -9, -11)
	07:30h	19:30h (NOAA-6, -8, -10, -12)

**Viewing Parameters:**

Scan Angle:	55.4° on either side of nadir
Total Swath Width:	2700 km
Ground Resolution:	1.1 x 1.1 km at nadir
	2.4 x 6.9 km at maximum scan angles

**Sensor Characteristics:**

Channel:	1	2	3	4	5
Spectral Range (µm):	0.5-0.68 <sup>b</sup>	0.725-1.10	3.55-3.93	10.3-11.3 <sup>c</sup>	11.5-12.5 <sup>d</sup>
IFOV <sup>e</sup> (milliradians):	1.39	1.41	1.51	1.41	1.30
S/N Ratio <sup>f</sup> :	3:1	3:1	-	-	-
Saturation:	100% reflectance for channels 1 and 2				
	320 K for channels 3 to 5				
Quantisation level:	10 bit precision for all channels				

<sup>a</sup> Local solar time<sup>d</sup> Not on NOAA-6, -8, -10<sup>b</sup> On TIROS-N: 0.55 - 0.90µm<sup>e</sup> IFOV: Instantaneous Field of View<sup>c</sup> 10.5 - 11.5µm for NOAA-6, -8, -10<sup>f</sup> Signal to noise ratio for 5% reflectance



Channel 1 (0.58  $\mu\text{m}$  to 0.68  $\mu\text{m}$ ) in the yellow/red part of the spectrum corresponds reasonably well with the spectral interval (0.6  $\mu\text{m}$  to 0.7  $\mu\text{m}$ ) recommended for green vegetation analysis, as it corresponds with the strong chlorophyll absorption band. Channel 2 (0.725  $\mu\text{m}$  to 1.1  $\mu\text{m}$ ) is potentially less satisfactory as it includes part of the chlorophyll absorption band as well as the more important highly reflective plateau in the near infrared (beyond 0.8  $\mu\text{m}$ ), which is associated with healthy green vegetation. Channel 3 (3.55  $\mu\text{m}$  to 3.93  $\mu\text{m}$ ), of the AVHRR is located near the spectral maximum for radiative emissions for objects radiating at temperatures around 800 K, i.e. the near-normal temperature for burning grass (Langaas and Muirhead, 1988), whilst channel 4 (10.3  $\mu\text{m}$  to 11.3  $\mu\text{m}$ ) and channel 5 (11.5  $\mu\text{m}$  to 12.5  $\mu\text{m}$ ) are located near the spectral maximum for normal environmental temperatures, around 300 K. As a consequence, in the case of burning grass (800 K) channel 3 will receive much more radiant energy than channel 4, and is therefore well suited to the detection of high temperature sources e.g. fire.

Full resolution AVHRR data (1.1 km) can be recorded for selected areas of the world in the LAC (Local Area Coverage) mode, or transmitted directly from the satellite in the High Resolution Picture Transmission (HRPT) mode for areas within a radius of 2500 km of a receiving station. Fire detection techniques are most reliable using these data (which can be requested on a daily basis) especially in areas where there is a good contrast between high temperature fires and cooler temperatures for the surrounding environment.

Lower resolution (4 km) GAC (Global Area Coverage) data are recorded on board, after resampling of the full resolution data. Even though the resampling (four out of five consecutive pixels are averaged for every third scan line) seriously affects the spatial and radiometric properties of the GAC data it offers the only currently available source of daily data (since 1981), at this spatial resolution for the entire globe. Belward (1991) has shown that this resampling scheme results in an unreliable spatial characterization of the environment, as well as in a strong bias for the detection of point phenomena, such as fires. When in full configuration, there are two NOAA satellites in complementary near-polar orbits, one crossing the equator at local solar times of approximately 07:30 and 19:30, and the other at 02:30 and 14:30. The orbital characteristics are such that with two satellites in operation, the possibility exists for twice daily and twice nightly coverage at any point on the equator. This coverage increases with latitude. This high temporal frequency has obvious benefits both for the detection and monitoring of fire events (which can vary in duration from two hours to several days) and in impact assessment studies of the affected vegetation.

The afternoon pass of the NOAA-AVHRR (14:30 equatorial crossing of NOAA - 11 and -13), is near-optimal in terms of fire detection and monitoring in the tropical belt, when winds tend to be stronger, the ground dew has evaporated and the vegetation is dry enough for efficient ignition. However, this does not preclude the possibility of missing fire events e.g. due to cloud cover, which can be at a maximum at this time over tropical regions.

Although Langaas (1992), used night-time AVHRR imagery (NOAA-10, 19:30-20:30 and NOAA-11, 01:30-02:30) to avoid problems such as channel 3 saturation and the unknown contribution of daytime reflected solar radiation to channel 3, a drawback

is that the satellite overpass time may be less optimal with respect to the time of maximum fire activity. In addition, even fires persisting for several days can show a strong diurnal cycle whereby they die down during the night and do not burn strongly again until the following afternoon (Belward et al. 1993). Night-time imagery therefore represents a very selective sample.

Dozier (1981) introduced a theoretical approach to the study of sub-pixel temperature fields using the AVHRR. He approximated the temperature field of each pixel by two areas of uniform temperature, the background area and a target area which occupies some fraction from 0 to 1 of the pixel. Using his model, Dozier was able to show that a sub-resolution high temperature target is detectable because it has a greater effect in channel 3 than in channel 4. Also based on his model, Dozier arrived at a pair of simultaneous, nonlinear equations that could be solved for the temperature and the size of the hot target given the background temperature and the brightness temperatures in channels 3 and 4. These equations, though, are restricted to pixels that are unsaturated in both channels. Background temperature is estimated from adjacent pixels and Dozier suggested using a split-window technique to calculate a correction factor for the effect of atmospheric water vapor.

The first applications of fire detection with AVHRR were to fixed targets of known location. Matson and Dozier (1981) used NOAA-6 imagery to detect high temperature industrial sources in Detroit and waste gas flares in the Persian Gulf. Similarly, Muirhead and Cracknell (1984) detected gas flares associated with oil fields in the North Sea using NOAA-6. In neither case were the details of the detection criteria discussed but presumably manual inspection of both channels 3 and 4 was an important component. An important difference between the two studies is that Muirhead and Cracknell (1984) used daytime imagery while Matson and Dozier (1981) used nighttime imagery, citing concern over the effects of reflected solar radiation in channel 3.

Following these studies of fixed targets, the AVHRR was used to detect vegetation fires. Matson et al. (1984) used daytime NOAA-6,7 imagery over the U.S. and Brazil to detect fires based on enhanced temperatures in channel 3. They also reported on an experimental operational fire monitoring project in the western U.S that was based on manual inspection of channel 3 and channel 4 images alternating on a screen. Most importantly, these detections were largely verified by Forest Service stations, timber companies and local police. Muirhead and Cracknell (1985) also looked at vegetation fires by applying their technique to the detection of straw burning in Great Britain using daytime NOAA-7 imagery.

The work of Flannigan and Vonder Haar (1986) and Flannigan (1985) represents the first attempt to use an automated (i.e. non-interactive) set of detection criteria. They used both daytime and nighttime data from NOAA-7 to monitor a severe forest fire outbreak in north-central Alberta, Canada. The detection criteria were based on manual inspection of a subset of the data and then applied in an automated fashion to the full dataset. Detection was based on a threshold channel 3-channel 4 brightness temperature difference of 8 K for nighttime data and 10 K for daytime data. They were also able to compare satellite detections with Alberta Forest Service daily reports which included fire location and size. These reports were based on late afternoon or early evening aerial reconnaissance. This allowed Flannigan and Vonder Haar not only to validate their ability to detect the presence of fires but also to apply the Dozier

equations and compare their calculated fire areas to the reconnaissance observations. Of the 41% of the fires that were visible to the satellite (unobstructed by smoke and cloud), 80% were detected by their detection criteria. Based on comparison with the reconnaissance information, the AVHRR-based fire size estimates were 70% too large for small fires and 50% too small for large fires.

A number of case studies were then reported from diverse regions (Matson et al. 1987, Matson and Holben 1987, Stephens and Matson 1989, Langaas and Muirhead 1989). While these studies did not focus on details of detection criteria and presumably involved interactive techniques, there was an increasingly sophisticated discussion of the limitations and problems associated with fire detection with the AVHRR. This included discussion of confusion from fixed, non-fire sources (Stephens and Matson, 1989), detection of and obstruction due to smoke plumes (Matson et al. 1987, Matson and Holben 1987), and problems associated with surface reflectivity and emissivity, pixel overlap at non-nadir scan angles and incorporation of recently burnt warm areas into the two-element temperature field of the Dozier model (Langaas and Muirhead, 1989).

Lee and Tag (1990) presented an alternative approach to non-interactive fire detection. Essentially they subjectively chose a threshold fire temperature and used the Dozier model to develop a look-up table specifying which combinations of satellite measurements constituted a positive fire detection. Atmospheric corrections were included in the estimation of background temperatures using the method of McClain et al. (1985). They applied their technique to nighttime imagery over the San Francisco area and the Persian Gulf.

Kaufman et al. (1990a,b) applied fire detection with NOAA-9 data to the estimation of emissions from biomass burning. Fires were detected in pixels that met three detection criteria. The first criterion was for the channel 3 brightness temperature to be elevated above a set threshold indicating a fire to be present. The second criterion specified that the channel 3 - channel 4 temperature difference must be at least 10 K and the third criterion used the channel 4 temperature to eliminate false detections from cool clouds that are highly reflective in the 3.8  $\mu\text{m}$  band.

Justice et al. (1996) and Scholes et al. (1996) combined AVHRR fire information in a dynamic model to generate improved trace gas and particulate emission estimates for Southern Africa. The approach combined satellite data on fire distribution and timing with fuel load calculated by a simplified ecosystem production model and ground based measurements of emission ratios (Ward et al. 1996, Shea et al. 1996). Daily fires detected by the AVHRR for the entire burning season were calibrated to provide burned area estimates using Landsat MSS data. The algorithm used for fire detection is described by Justice and Dowty 1994 and is the basis for the IGBP-DIS community consensus algorithm for the AVHRR. This trace gas modeling was part of a larger body of fire related research as part of the IGBP Southern African Fire Atmosphere Research Initiative (SAFARI) (Andreae et al. 1995).

Setzer and Pereira (1991a) describe an operational fire monitoring program in Brazil. Using NOAA-11 data in 1989, 96% of detected fires were verified by ground crews and there were no reports of missing fires. Setzer and Pereira (1991b) used a fixed channel 3 temperature threshold to flag potential fires but also required that a smoke plume be visible in channel 1 for there to be a positive detection. In order to get

a regional estimate of burned area over a burning season, they used a comparison of NOAA-9/AVHRR and Landsat/TM to determine an average fire size, 0.72 of an AVHRR pixel, and assumed that the average duration of a fire was 1.5 days.

Periera et al. (1991) used AVHRR data from five consecutive days and Landsat/TM data from the sixth day to evaluate the accuracy of fire detection and burned area estimates. All AVHRR-detected fires had corresponding TM scars. When assuming that an AVHRR-detected fire burned the entire pixel, the fire size was overestimated on the average by 43%.

Cahoon et al. (1991) examined a large fire in China using NOAA-9 data. Using 3.7  $\mu\text{m}$  saturation as their detection criteria, they found good correspondence with observed smoke plumes. In contrast, Brustet et al. (1991) reported on an AVHRR study in semi-arid West Africa. They found that a threshold in the 3.7  $\mu\text{m}$  channel alone was adequate for fire detection in some cases, while for dry vegetation and a hot background surface, a second threshold applied to the 11  $\mu\text{m}$  channel was necessary. Techniques developed for vegetation fires can also be used in an urban setting as shown by Doussett et al. (1993) through the detection of fires following rioting in Los Angeles in April 1992. Robinson (1991), Kennedy (1992), Justice and Malingreau (1994), and Giglio et al. (1998) all provide reviews of fire detection with AVHRR and address a number of sources of uncertainty.

#### 2.2.5.2 AVHRR fire detection techniques.

The primary data available consists of the measurements in all five AVHRR channels from a) the pixel being evaluated, b) the pixels contained within some spatial window about the central pixel and c) the pixels in some temporal series that includes the particular scene being evaluated. Secondary data that may be available include surface reflectance (or emissivity), some measure of water vapor in the atmospheric column, aerosol optical depth and information concerning the location of permanent non-biomass burning heat sources, such as oil refineries. Most algorithms utilize a subset of the primary data and none of the secondary data (the GOES ABBA procedure is an exception). In general algorithms utilize one or more of the following:  $T_3$ ,  $T_4$ ,  $T_{34}$  ( $T_3 - T_4$ ) and some characterization of the background in a spatial window about the pixel being evaluated.

A 'fire signal' can be generally thought of as an enhancement in channel 3 relative to the background. There will be some level of variability, though, in the background brightness temperature as measured in channel 3. For increasingly smaller and cooler fires, the magnitude of the fire signature will decrease until it is indistinguishable from the background variability. At some point there must be a theoretical lower detection limit, applicable to all detection algorithms, that is a function of the amplitude of the background variability. Also, a practical lower detection limit exists, distinct from the theoretical limit, that reflects the ability of a particular algorithm to resolve a fire signature from the background variability. Similarly, algorithms that depend on enhanced  $T_{34}$  for fire detection will have an upper detection limit. Fires larger and hotter than the detection limit will lead to sensor saturation and decreased values of  $T_{34}$ . Theoretical simulations indicate that both upper and lower detection limits vary among the fire detection techniques (Dowty 1993, Giglio et al. 1998).

Clearly it is important to identify non-fire factors that cause variability in the IR signal as detected by the AVHRR, particularly those that enhance the response in channel 3. Cooper and Asrar (1989) report a 6 K enhancement of channel 3 over channel 4 in the absence of fire. Simulation studies suggest that extreme cases may lead to a 15 K enhancement (Dowty 1993). Factors that may be responsible for such effects include the water vapor content of the atmosphere, reflection of solar radiation in the 3.75  $\mu\text{m}$  band, occurrence of sub-resolution land cover anomalies (with associated emissive and reflective properties) and occurrence of sub-resolution clouds. Some factors will act over a relatively large area and potentially can be accounted for through spatial analysis, e.g. atmospheric water vapor. Others may have isolated, sub-resolution occurrences and be more difficult to account for, e.g. isolated, sub-resolution cloud. Some algorithms based only on  $T_{34}$  thresholds produce false detections at cloud edges because there are a number of pixels only partially filled with cloud. The proportion of cloud may be small enough so that the pixel slips through the cloud screen but large enough so that the channel 3 response is significantly enhanced by highly reflective clouds.

The channel 3 response in daytime data may be strongly enhanced by surface reflection where the satellite-surface-solar geometry results in sunglint. This effect has been documented over oceans (Nath et al. 1993, Cracknell 1993) and can lead to false fire detections over land (Alberto Setzer, pers. comm.). Setzer noticed that for a very sharp ocean glint (low wind speed), while the reflectance in channel 1 and 2 continued to increase toward the center of the glint, above a given threshold the channel 3 stopped increasing and decreased slightly. Apparently radiance larger than the saturation threshold in channel 3 causes a decrease in the channel 3 value rather than a constant saturated value. It appears that intense fires above saturation level will have a slightly lower value than intense fires.

Pixel overlap at high scan angles is an issue that has important implications for fire detection. At the edge of a scan, over 60% of the area viewed within a pixel is also viewed by adjacent pixels (Cahoon et al. 1992a). This could lead to replicate counting of fire events and decreases the value of extreme off-nadir data. At present, no techniques have been developed to account for pixel overlap effects apart from reducing the portion of the scan that is used.

Finally, the effect of temporal sampling is an important issue in fire detection with AVHRR data. Presently there are four potential AVHRR sampling times; one daytime and one nighttime pass for each satellite (NOAA-11 and NOAA-12). Rarely, however, is all this data available and most fire detection studies use only one satellite pass. This pass is then used to represent the burning events for an entire day. It is important to consider the diurnal pattern of burning and the timing of the NOAA satellite overpass in order to understand the limitations of using one temporal sample. In this regard, comparison of AVHRR-derived fires with GOES-derived fires can be very useful (see Section 2).

In the following text we review a number of existing AVHRR algorithm approaches for the detection of active fires. These are grouped as fixed threshold techniques, the Lee and Tag technique, and spatial analysis techniques. Although cloud screening procedures are typically integrated with fire detection, the cloud screening steps are not discussed here.

### Fixed Threshold Techniques

There are a number of approaches which compare AVHRR data with various fixed thresholds to determine whether a pixel is to be classified as a fire pixel. A threshold value of the channel 3, channel 4 difference ( $T_{34}$ ) is often used, sometimes in conjunction with a threshold applied to the individual value in channels 3 or 4.

The method of Flannigan and Vonder Haar (1986) consisted of the following tests over a forested region:

- a)  $T_3 > T_{3b}$
- b)  $T_4 > T_{4b}$
- c)  $T_{34} > 8 \text{ K (nighttime)}$   
 $T_{34} > 10 \text{ K (daytime)}$

where  $T_{3b}$  and  $T_{4b}$  are average values from neighboring pixels. The first two tests require that a fire pixel be hotter than the background and the third test compares  $T_{34}$  to a threshold. A higher threshold was used during the day because of reflective and surface heating effects. This approach includes spatial analysis in the form of  $T_{3b}$  and  $T_{4b}$ , but is classified here as a fixed threshold technique because of the third, more critical, test. A cloud screening was performed separately based on Coakley and Bretherton (1982).

Kaufman et al. (1990a,b) used three tests to detect deforestation fires in Brazil:

- a)  $T_3 \geq 316 \text{ K}$
- b)  $T_{34} \geq 10 \text{ K}$
- c)  $T_4 > 250 \text{ K}$

The first test ensures that the pixel be hot. The second test is the same as that used by Flannigan and Vonder Haar (1986), and the third is intended to screen out clouds that may be reflective in the channel 3 band but are cool in channel 4.

A number of studies in Brazil base detection on a channel 3 threshold alone, sometimes with a requirement that a smoke plume be visible in channel 1. Setzer and Pereira (1991b) detected deforestation fires using

- a)  $T_3 > 319 \text{ K}$
- b) manual detection of smoke plume in channel 1

Pereira et al (1991) and Pereira and Setzer (1993) also used a channel 3 threshold alone and examined raw digital counts instead of derived brightness temperatures. Pereira et al. (1991) required that channel 3  $\geq 10$  (raw digital counts) on an 8-bit (256) scale where the 8 most significant bits of the original data are used. Pereira and Setzer (1993) required that channel 3  $\geq 8$  (raw digital counts) on the same scale. These studies used daytime data.

Franca et al. (1993a, b) used the following five tests to detect fires in West African savannas in daytime imagery:

- a)  $T_3 > 320 \text{ K}$
- b)  $T_{34} \geq 15 \text{ K}$
- c)  $T_4 > 287 \text{ K}$
- d)  $0 \leq T_{45} \leq 5 \text{ K}$
- e)  $A_1 < 9\% \text{ reflectance}$

where  $A_1$  is the reflectance in channel 1 and  $T_{45}$  is the difference between channels 4 and 5. The first three tests are similar to those of Kaufman (1990a,b) and the last two tests increase the ability of the algorithm to discriminate cloud, particularly sub-resolution cloud.

Many of the fixed threshold studies discussed above included some type of validation exercise and each of these reported good results. The fixed threshold approach seems very appropriate and performs very well within specific study areas. It must be kept in mind, though, that each of these fixed threshold algorithms was optimized for a particular region. If an algorithm is applied to a region outside that for which it was designed, presumably it would require some modification.

### Lee and Tag Technique

The approach described here is that of Lee and Tag (1990), although the implementation is slightly modified here. They essentially compare an adjusted channel 3 brightness temperature to a threshold value that is selected on a pixel-by-pixel basis. This threshold is calculated as a function of a derived background temperature and an adjusted channel 4 brightness temperature by using Dozier's model. This method can be divided into three steps:

**Step 1:** Background temperatures are estimated and adjusted brightness temperatures are calculated.

- a) The brightness temperatures from pixels adjacent to the pixel being tested are averaged. This is actually done once with corner pixels and once with side pixels and the final results are then compared for consistency. Each channel is averaged separately resulting in three 'background' values:  $T_{3b}$ ,  $T_{4b}$  and  $T_{5b}$ .
- b) The atmospheric correction algorithm of McClain et al. (1985) is used with  $T_{3b}$ ,  $T_{4b}$  and  $T_{5b}$  to calculate an estimate of background land surface temperature  $T_b$ .
- c) Three correction factors are calculated by subtracting  $T_{3b}$ ,  $T_{4b}$  and  $T_{5b}$  from  $T_b$ .
- d) These correction factors are added to the observed brightness temperatures of the pixel to obtain adjusted values for channels 3 and 4,  $T_3^*$  and  $T_4^*$ . The idea here is that the brightness temperature of adjacent pixels with no fire should match the background temperature. Any deviation can be attributed to factors (atmosphere, surface reflectance, etc.) that would affect the central pixel also.

**Step 2:** The threshold channel 3 brightness temperature is calculated. Dozier's model is used here to relate surface parameters (fire size, fire temperature and background temperature) to AVHRR observations. A threshold fire temperature,  $T_{min}$ , must be specified which represents the minimum fire temperature of interest. The size of a fire at the threshold temperature is found so that the predicted channel 4 brightness temperature matches the adjusted observed value,  $T_4^*$ . The corresponding brightness temperature predicted for channel 3 is used as a threshold.

**Step 3:** If the adjusted channel 3 brightness temperature,  $T_3^*$ , is greater than the threshold then the pixel is flagged as a 'fire pixel'.

### Spatial Analysis Techniques

These techniques employ variable thresholds that are derived on a pixel-by-pixel basis from the information contained in some spatial window about each pixel. These are to be distinguished from the Lee and Tag approach because here the thresholds are empirically or statistically determined whereas the Lee and Tag variable thresholds are based on theoretical calculations.

The Automated Biomass Burning Algorithm (Prins and Menzel, 1993), applied to GOES VAS data, is an example of the spatial analysis approach (see Section 2). A similar approach was developed at NASA/Goddard Space Flight Center for use with AVHRR 1 km data. An important part of both of these algorithms involves a comparison of the  $T_{34}$  value for each pixel with a threshold that is determined on a pixel-by-pixel basis. The threshold is a function of the standard deviation of  $T_{34}$  in a spatial window about each pixel. This explicitly ties the detection criteria to the variability in the background.

In the Goddard algorithm, pixels are flagged as 'potential' fire pixels if:

- a)  $T_3 \geq 316 \text{ K}$
- b)  $T_4 \geq 290 \text{ K}$
- c)  $T_3 > T_4$

This eliminates a large number of pixels from further consideration and reduces processing time. The  $T_{34}$  value of each 'potential' fire pixel is then compared to a threshold that is determined from the background, or neighboring pixels. This threshold is equal to the mean value of  $T_{34}$  of the background pixels plus twice the standard deviation of  $T_{34}$  of the background pixels. There is an additional stipulation that the threshold must be greater or equal to 3 K, otherwise it defaults to 3 K. If  $T_{34}$  of a potential fire pixel is greater than the resultant threshold, it is classified as a fire pixel.

The mean and standard deviation are determined from the background pixels as follows. Background pixels that are themselves potential fire pixels are not included in the calculation of background statistics. The size of the background 'window' is allowed to migrate from a 3 by 3 pixel box (the eight surrounding pixels) up to a 21 by 21 pixel box as necessary until at least 25% of the background pixels are available for the calculation of background statistics. There must be at least 3 pixels used in the calculation. If the background statistics cannot be calculated then the central pixel cannot be classified as a fire pixel.

While the potential for AVHRR fire products are significant, there are also serious problems, limitations and unresolved issues associated with AVHRR data and fire detection procedures. A fundamental problem with fire detection is that it is limited to cloud-free areas. This can be a serious problem in areas of high cloudiness. A number of phenomenon affect the IR signal received by the AVHRR and hence may confuse or confound fire detection (Giglio et al. 1998). These include surface reflection of solar radiation in the  $3.75 \mu\text{m}$  band and the effects of atmospheric water vapor and sub-resolution cloud. The viewing geometry of the AVHRR gives rise to variable pixel size and pixel overlap issues that complicate the interpretation of detected fires. All



these issues need more attention in the context of developing a MODIS operational procedure.

### 2.3 MODIS INSTRUMENT CHARACTERISTICS ASSOCIATED WITH THE FIRE PRODUCT.

The MODIS 1 km 4  $\mu\text{m}$  high gain channel was specified to have a saturation level of 500 K with NE  $T$  of 0.3 K. This channel is not affected by water vapor absorption and only weakly affected by other gaseous absorption (see Fig. 1).

The MODIS 11  $\mu\text{m}$  channel, with a 1 km resolution, saturates at a temperature of 400 K, with NE  $T$  of 0.1 K. Detection may be also possible at night using the 0.86  $\mu\text{m}$  channel which has a 250 m resolution and 2.1  $\mu\text{m}$  and 1.6  $\mu\text{m}$  channels, with a 500 m resolution, though there are however no plans for routine collection of the solar channels during the night. The MODIS design tries to ensure the highest possible locational accuracy of the data to provide the best information as to the location of fires and to allow multitemporal monitoring of fires. Good band-to-band registration (0.1 of a pixel) and scene to scene registration is required, since misregistration will lead to overestimation of fire occurrence. Since there is no possibility for on-board calibration of the fire channels at high temperatures, detailed preflight calibration is planned, as well as in-flight vicarious calibration using known fixed sources such as gas flares.

The MODIS 250 m bands can be used to provide information on the spatial variability of the 1 km fire pixel and the background surface. An inverse relationship has been established between the NDVI and surface temperature, which may help with assumptions concerning background temperature. The MODIS cloud mask will be an important component of the fire detection to identify areas where the surface is obscured by clouds and fires are undetectable. The 250 m channels will also be used to detect sub-pixel clouds within the 1 km pixel. The MODIS sensor scans the Earth with 10 simultaneous 1 km wide stripes (or 20 and 40 stripes at the 500 m and 250 m resolutions respectively). The general design of the MODIS instrument and its application for remote sensing are described in Salomonson et al. (1989); King et al., (1992) and Running et al (1994). At off-nadir there is an overlap between the scan lines of different swaths. To avoid the effect of off nadir viewing on multiplicative fire detection, we shall limit the fire detection to view angles within  $\pm 45^\circ$ .

The MODIS pixel size at 4  $\mu\text{m}$  and 11  $\mu\text{m}$  is 1 km. However, due to the scanning mode of MODIS, the response is triangular across 2 km with maximum response in the center of the pixel (see Fig. 2). As a result, fires can be expected to be detected by two adjacent pixels depending on the location of the fire relative to the pixel and on the strength of the fire. Note that if instead of a triangular response the MODIS response would be rectangular with no overlap, each fire would be singularly detected with a response equal to the sum of the responses of the two adjacent pixels depicted by the triangular response.

### 2.3.1 MODIS FIRE PRODUCT PROTOTYPING ACTIVITIES: APPLICATION TO WILD AND PRESCRIBED FIRES

#### 2.3.1.1 Landsat observations of the 1988 Yellowstone Fire

The Yellowstone fire in Wyoming, Montana, and Idaho began with a series of lightning strikes on July 9 - 11, 1988 and eventually spread to engulf 5,000 km<sup>2</sup> in and around the Yellowstone National Park. (Morrison, 1992). A Landsat TM image was acquired on September 8, 1988 at 10:30 and is used here to describe the wildfire and to simulate MODIS fire observations. The Landsat TM sensor has 7 spectral channels, six with a resolution of 30 m: 0.48  $\mu$ m, 0.56  $\mu$ m, 0.66  $\mu$ m, 0.83  $\mu$ m, 1.65  $\mu$ m, and 2.2  $\mu$ m and one with a resolution of 120 m at 11  $\mu$ m. Figure 4 shows the entire Yellowstone data set (216 km x 180 km) resampled to the MODIS spatial resolution of 500 m/pixel and converted to simulate MODIS channels at 2.2  $\mu$ m, 1.65  $\mu$ m, and 0.66  $\mu$ m using red, green and blue respectively. The image is useful for identifying a chronology of fire activity. Pink areas are regions of intense active fires, while brick-red areas represent burn scars that are 1 to 3 days old where smoldering elements and small fire pockets are still radiating significant amounts of flux at 2.2  $\mu$ m. Older burn scars are included in the yellow areas of the image. Thus, MODIS channels at 2.2  $\mu$ m, 1.65  $\mu$ m, and 0.66  $\mu$ m could be used to estimate the extent of active fires and recent burn scars while smoke enshrouds the area of interest.

As a background to the satellite observations, we shall describe the fire development of the preceding day for a small subsection of Yellowstone (Figures 3 and 4; see also Flynn and Mougini-Mark, 1995). Twenty-four hours before the TM pass there were two large columns of smoke and fire 5 km west and southwest of the location of the Yellowstone Old Faithful geyser. At 03:00 on September 7, the winds began to strengthen from the southwest. At 03:30, the fire was close to the Old Faithful Visitor Center with strong enough convection to generate winds of 80 km/hr towards the fire. Fire balls and flaming elements passed to the northeast of the visitor center (Morrison, 1992). That particular fork of the fire zone (shown 20 km west of Yellowstone lake in Figure 4) grew by 200 km<sup>2</sup> that day.

Figure 5a is a false color composite of the 11.4  $\mu$ m (red), 2.2  $\mu$ m (green), and 1.65  $\mu$ m (blue) TM channels which shows the location of the fire and the burned area. The burn scars are warmer than the surrounding area and are therefore, shown in pink-red colors. The large burn scar in the lower right part of the image was generated by a fire storm 19 hours before the acquisition of the TM image. It is 2.1 km wide at the base and 12.7 km long. Many of the active fires located mainly along the perimeter of the burn scar saturated the 2.2  $\mu$ m channel. The active fire cells appear yellow-white in the image and are relatively small (60 - 120 m) with the largest one 300 m across. Table 4 gives the typical values of reflectance at 1.6  $\mu$ m and 2.1  $\mu$ m and temperature at 11  $\mu$ m of the yellow-white fire spots, the burn scar, and the background.

Table 4: Typical reflectance and temperature characteristics of the Yellowstone fires

Wavelength	Fire Condition	Reflectance	Temperature (K)
1.65 $\mu\text{m}$	active fire	0.503	
	burn scar	0.139	
	background	0.122	
2.2 $\mu\text{m}$	active fire	0.913	
	burn scar	0.188	
	background	0.067	
11 $\mu\text{m}$	active fire		325
	burn scar		317
	background		303

Figure 5b is a composite of the 11  $\mu\text{m}$  (red), 0.66  $\mu\text{m}$  (green), and 0.48  $\mu\text{m}$  (blue) channels, showing the position of the burn scars relative to the smoke plumes generated from the more intense fires. Comparison of the two figures shows the relationship between the presence of main fires and the emission of smoke.

Figure 6 shows another simulation of the MODIS response to the Yellowstone fire. Since the TM does not have a 4  $\mu\text{m}$  channel which is the main fire channel on MODIS, we generated it from the non-saturating TM channels (1.65  $\mu\text{m}$ , 2.2  $\mu\text{m}$ , and 11  $\mu\text{m}$ ). The figure shows on the left a false color composite of the 11  $\mu\text{m}$  (red), 4  $\mu\text{m}$  (green), and 1.65  $\mu\text{m}$  (blue) in full TM resolution. On the right the same color picture is shown but after the resolution was reduced to 1 km. The same spatial distribution of the information is seen, though it is intuitively less clear due to the reduced resolution. Quantitative comparison between the thermal energy derived from the simulated MODIS observations and the Landsat observations are shown in Figure 7. The thermal energy is derived from the simulated 4  $\mu\text{m}$  channel in both cases. For the TM, the thermal energy was derived from individual 30 m pixels and averaged to the 1 km resolution. The thermal energy derived from the simulated MODIS image is plotted in the figure as a function of the thermal energy derived from the TM image. In Fig. 7a the MODIS data are for a hypothetical rectangular 1 km response, and in Fig. 7b for the triangular response. The plots in Fig. 7 show the effect of the reduced MODIS resolution on the detection of fires and the derivation of thermal energy. The reduced resolution retains the basic information on the thermal energy, though the derived energy is larger than the "true" energy generated from the higher resolution data. This difference is due to the inhomogeneity of the temperature field and the non-linearity between the fire radiance and energy.

The conclusion from this application of the MODIS concept to the Yellowstone fire data is that this type of wildfire will be clearly observed from MODIS and that the thermal energy can be calculated from the MODIS pixel, though it will be significantly larger in some instances than the energy that could have been detected with high resolution sensors. This demonstrates that the database of MODIS thermal energy will be useful for comparison between fires but cannot be used in an absolute sense unless

correlated with some additional quantity, such as the emission of burning products. This is the subject of the next application.

#### 2.3.1.2 MODIS Airborne Simulator data of prescribed fires in the SCAR-C experiment

The SCAR-C (Smoke Cloud and Radiation - California) experiment was conducted in September 1994 in the Northwest US (Kaufman et al., 1996). In the experiment, the entire process of biomass burning was measured, including ground-based estimates of fuel consumption, airborne sampling of the smoke aerosol and trace gases, and air-borne and spaceborne remote sensing of both the fires and the smoke. In this simulation study we use remote sensing data collected during the experiment by the MODIS Airborne Simulator (MAS) flown on NASA's ER-2 aircraft, to find if there is a relationship between the fire emission of thermal energy and emission of smoke and trace gases. The MAS scans in the crosstrack direction in 35 km swaths collecting data with a nominal 45 m resolution (King 1994). For SCAR-C, MAS was configured with 11 spectral channels that included the 0.66  $\mu\text{m}$ , 1.6  $\mu\text{m}$  and 4  $\mu\text{m}$  channels used in this study. Several prescribed and wild fires were measured. The Quinault prescribed fire on the coast of Washington State (Sept. 21, 1994) was the best measured example of the relationship between the fire rate of emission of thermal energy and the rate of emission of particulates. Both the fire thermal energy and emission of particulates were remotely sensed by MAS. Fire thermal energy was monitored by the 1.6  $\mu\text{m}$  and 4  $\mu\text{m}$  channels, while emissions of smoke were measured independently, in 0.66  $\mu\text{m}$  downwind from the fire. The fuel that fed the Quinault fire consisted of the dry remnants of large western red Cedar debris, left over from logging. The density of the fuel, including the deep forest floor of accumulated woody material, was 38 kg/m<sup>2</sup>, about half of it (22 kg/m<sup>2</sup>) was consumed in the burn according to US Forest Service report. The burn site was reported by the US Forest Service to be 0.2 km<sup>2</sup>, while remote sensing at 4  $\mu\text{m}$  found a similar size of 0.25 km<sup>2</sup>. The fire was ignited by heliotorch at 18:10 GMT and immediately burned vigorously, continuing for about 6 hours.

The ER-2 flew over the fire eight times, each time generating an image of the size and apparent temperature of the fire and an image of the smoke plume. Fig. 8 shows the first of such remote sensing images taken from the ER-2 of the fire temperature and the emitted smoke. The size of the fire was monitored using the 4  $\mu\text{m}$  channel which proved to be the most sensitive to the temperature anomaly. However, this channel saturated at 450 K. As a result, at the MAS resolution the fire thermal energy was monitored by a combination of the 4  $\mu\text{m}$  channel and the 1.6  $\mu\text{m}$  channel. Since the 1.6  $\mu\text{m}$  is sensitive only to temperatures above 620 K, there is a gap between the two channels with low sensitivity. The 1.6  $\mu\text{m}$  channel saturates at 860 K. For the high spatial resolution of the imagers, this channel is very sensitive to the presence of flaming and gives a high resolution image of the fire. The use of the 1.6  $\mu\text{m}$  channel is different from that of the MODIS 4  $\mu\text{m}$  channel, but demonstrates the application of the use of rate of emission of thermal energy derived from remote sensing. This channel was calibrated on the ground before flight, and the calibration was compared and updated using simultaneous AVIRIS data.

Application of the MAS images of the fire and smoke acquired in the Quinault fire are shown in Fig. 9. The figure shows the rate of emission of thermal energy from the fire and the rate of emission of particulates. The rate of emission of thermal energy is calculated from the difference between the detected radiance at  $1.6 \mu\text{m}$ , and the radiance due to reflection of sunlight. It is converted to the rate of emission of thermal energy assuming that each 45 m pixel is a homogeneous black body. To calculate the rate of smoke emission, we followed the procedure of Fraser et al. (1984) developed for the calculation of the flux of sulfate exiting the US coast to the Atlantic. The average smoke brightness at  $0.66 \mu\text{m}$  was converted into the smoke optical thickness using a radiative transfer lookup table that describes the relationship between the optical thickness and the upward radiance at the top of the atmosphere for a plane parallel smoke model (Kaufman et al., 1996). The smoke optical thickness ( $\tau$ ) was converted to the smoke mass density ( $M$ ) using a conversion factor of  $\tau = 0.11 \text{ g/m}^2$  for the dry part of the smoke ( $M = \tau / 0.11$ , Kaufman et al. 1990a). The rate of emission was calculated for an average wind speed of  $7 \pm 2 \text{ m/s}$ . The wind speed was obtained from 6 consecutive observations from the MAS images of the distance of the edge of the smoke plume from the fire. Figure 9 shows that the rate of emission of smoke and the rate of emission of thermal energy, evolve as a function of time in a remarkably similar way. This shows that at least in the case of this fire, there is a direct relationship between the rate of emission of thermal radiation from the fire and the rate of emission of smoke. We plan to apply this procedure to the rest of the fires measured during the SCAR-C experiment and to hundreds of fires in Brazil measured during the SCAR-B experiment in 1995. We also plan to use indoor laboratory fires to establish, in a controlled environment the relationship between the fire thermal energy and rate of emission of aerosol and trace gases.

#### 2.3.1.3 AVHRR prototyping of MODIS global active fire products.

The IGBP Global 1km Project provides an important prototype for MODIS data products and is described by Townshend et al (1995) and Eidenshink et al (1995). Data are being collected from a number of ground stations around the World and contributed to a global archive. As part of the NASA EOS program the global daily AVHRR data have been compiled at the Eros Data Center from April 1992 to the present. The daily orbits can be processed to identify fires and can be combined to show the global distribution of fires. The IGBP-DIS Fire Working Group developed a community consensus AVHRR algorithm that was applied to eighteen months of daytime daily AVHRR data. The algorithm is described in Flasse and Ceccato (1996). This data set provides a useful tool to evaluate the global distribution and timing of fires to be identified by the MODIS. It is important to note that several of the limitations of the AVHRR for fire sensing described above will be overcome by the MODIS instrument.

## 2.4 INTENDED FIRE PRODUCT USER COMMUNITY

The intended user community for the MODIS products are those scientists requiring information on fire distribution, timing, and characteristics for inclusion in

modeling studies. Fire data are currently being used to drive regional emissions models, trace gas transport models and mesoscale models of atmospheric chemistry and global models of aerosol forcing. The data requirements from these communities vary widely from daily fire distributions over selected regions to global summaries of fire distribution at different temporal and spatial resolutions. The modeling efforts are currently constrained by the limited accuracy of the fire detection techniques which is directly related to current sensor limitations. As the existing fire data sets become more widely available we envision that the data will be used as an input to regional scale ecological process models. To meet the immediate needs of the science community requiring estimates of area burned, it will be necessary to establish the relationship to detected number of fires and the associated area burned. Such calibrations are currently being developed from the AVHRR using multitemporal high spatial resolution Landsat data.

In addition to the modeling community, data on fire distribution and frequency will be of use to those addressing questions of natural resource management. However at present it is not the intention of this product to provide real time data for fire management purposes. Discussion is needed with scientists monitoring volcano activity to see if the MODIS fire products can meet their scientific data needs for near real-time products or whether a separate rapid processing stream is required.

## 2.5 AN EXAMPLE OF THE USE OF SATELLITE DERIVED FIRE CHARACTERISTICS.

Modeling of the impact of fires on atmospheric composition, based on remote sensing, may take the following path for a given ecological region:

- During the burning season collect information (from MODIS) on the fire occurrence and distribution as a function of the fire strength (related to combustion rate). Add to this information the diurnal cycle of the fires from observations from geostationary satellites (Menzel et al., 1991) of the fires and the smoke emitted from them, observations of smoke from MODIS and ground based observations.

- Determine the expected fire efficiency and/or smoldering to flaming ratio in order to be able to estimate the emission rates per fire and emission ratios. This information could be constructed as a combination of observations from MODIS of the fires, of smoke (emitted particulates - Kaufman et al., 1990a and b) and ground-based monitoring.

For example the total amount of trace species  $i$  (e.g. particulates, CO, CO<sub>2</sub> or CH<sub>4</sub>),  $M_i$  from a given region and period of time (in mass units) can be determined from the following formula:

$$M_i = \sum_{c=1}^n N_c M_{ic} m_{ic}$$

The summation is over  $n$  classes of fires determined based on the fire strength:

- $N_c$  is the number of fires in the class in the given region and period of time,
- $M_{tc}$  is the average rate of combustion of organic material in fires in the class (estimated from empirical relationships between ground based observations and the MODIS fire detection or from comparison of the rate of emission of particulates from the fire and the fire class for specific fires).
- $m_{ic}$  is the fraction of carbon mass in the fuel emitted as trace element  $i$  derived for the average ratio of smoldering to flaming in the class.
- $\tau_c$  is the average lifetime of the fire for the present emission rate, estimated from geostationary satellite data, or ground based observations or observations of the emitted particles from the satellite platforms.

### 3.0 MODIS ALGORITHM DESCRIPTION

#### 3.1 THEORETICAL DESCRIPTION

The MODIS fire detection and characterisation techniques are planned to be fully automated for the production of daily, global fire information. In order to detect the presence of fire in a non-interactive fashion, a set of detection criteria different for the day and night fire observations are prescribed. These multipsectral criteria are based on the apparent temperature of the fire pixel and the difference between the fire pixel and its background temperature.

##### 3.1.1 PHYSICS OF THE PROBLEM

Amongst the fire characteristics planned for estimation using MODIS, the determination of the flaming and smoldering ratio is perhaps the most challenging and warrants some extended discussion. The two fire stages, flaming and smoldering, distinct for example in forest fires, are characterized by different fire intensity, temperature, and emission ratios. In several field experiments in Brazil, Ward et al., measured 2-3 times as much emission of aerosol particles,  $CH_4$  and NMHC in the smoldering phase as in the flaming phase (Ward et al., 1992; Kaufman et al., 1992; Malingreau et al. 1993). Therefore it is important to be able to distinguish between these two phases.

Smoldering and flaming can be distinguished using IR remotely sensed measurements only if the fire temperatures vary significantly between these two stages. Based on review of the fire properties by Lobrt and Warnatz (1993) flaming temperature can be anywhere between 800 K and 1200 K and as hot as 1800 K. Smoldering should be under 850 K and above 450 K. The actual range is probably smaller. Therefore we shall base the algorithm and sensitivity studies on the assumption that the flaming temperature is  $1000\text{ K} \pm 200\text{ K}$  and smoldering  $600\text{ K} \pm 100\text{ K}$ .

In a given fire pixel we may have areas that are not burned, areas that are smoldering and areas that are in flames. Figure 10 demonstrates the sensitivity of the potential MODIS channels to the fraction of the pixel covered by flames of 1000 K ( $f_{\text{flame}}$ ), and a fraction of the pixel covered by smoldering of 600 K ( $f_{\text{smold}}$ ). The rest of

the pixel has a temperature of 300 K. The shorter the wavelength, the stronger the sensitivity to the higher temperature region. The main results of the simulation are summarized in Table 5.

Table 5: Information on the MODIS bands that can be used for fire detection. The saturation is given in reflectance units for the reflective bands ( ) or in temperature units (T) for the emissive bands. The sensitivity is given in degrees change ( T) per change in the area covered by fire (f) or in change in the apparent surface reflectance ( ).

channel	spatial resolution	saturation	fraction of pixel that saturates the channel		sensitivity ( T/ f) and ( T/ E <sub>f</sub> ) of smoldering at 600 K	sensitivity ( / f) and ( / E <sub>f</sub> ) of flaming at 1000K
1.65 μm	500 m	= 1 (740 K)	0.05	no saturation	/ f=0.064 / E <sub>f</sub> =9·10 <sup>-6</sup>	/ f=220 / E <sub>f</sub> =5·10 <sup>-4</sup>
2.13 μm	500 m	= 0.8 (570K)	0.007	0.65	/ f=1.2 / E <sub>f</sub> =2·10 <sup>-4</sup>	/ f=110 / E <sub>f</sub> =3·10 <sup>-4</sup>
4 μm	1000 m	500 K	0.025	0.30	T/ f=800 T/ E <sub>f</sub> =0.11 at f=0.05	T/ f=8300 T/ E <sub>f</sub> =0.02 at f=0.005
11 μm	1000 m	400 K	0.07	0.25	T/ f=480 T/ E <sub>f</sub> =0.07 at f=0.05	T/ f=1700 T/ E <sub>f</sub> =0.004 at f=0.005
energy, E <sub>f</sub> (MWatt)					E <sub>f</sub> / f=7300	E <sub>f</sub> / f=430,000

The 1.65 μm channel is very sensitive to  $f_{\text{flame}}$  and the flaming energy and not very sensitive to  $f_{\text{smold}}$  and its energy. The 2.13 μm channel is very sensitive to  $f_{\text{flame}}$  and somewhat sensitive to  $f_{\text{smold}}$ . Since the thermal energy is more concentrated in the flaming fire, the sensitivity to thermal energy is independent of smoldering or flaming. Unfortunately the MODIS 2.13 μm channel saturates at a reflectance of 0.8, which for the low solar brightness in this channel corresponds to less than 1% of the 500 m pixel being in flames. The importance of this channel is therefore limited. The 4 μm channel is sensitive to both  $f_{\text{flame}}$  and  $f_{\text{smold}}$ , and is 5 times more sensitive to the thermal energy emitted from flaming than from smoldering, Fig. 11 shows the effect of a fire size and temperature on the apparent temperature of the pixel at 4 μm. This channel is sensitive to fires as small as 10<sup>-4</sup> of the fire pixel.

The 4 μm channel response in daytime may be strongly enhanced by surface reflection where the satellite-surface-solar geometry results in sunglint. This effect has been documented over oceans (Nath et al., 1993; Cracknell, 1993) and can lead to false fire detections over land (Alberto Setzer, pers. comm.). Therefore the MODIS fire algorithm tests for sun glint and excludes those pixels from the fire products.

The following procedures emerge from the physics of fire thermal emission discussed above and the algorithms used with currently available AVHRR and GOES



data. Only the procedures using the 4  $\mu\text{m}$  and 11  $\mu\text{m}$  bands are described. In its current form, a number of threshold values are included. These values are given for both day and (night) observations. During the night the signal in 4  $\mu\text{m}$  is smaller due to lack of reflection of sunlight and the thresholds are lower. The regional and seasonal variability of the land surface makes absolute thresholds undesirable. The threshold values presented below were subjectively determined, based on the cited literature and the present remote sensing experience of the authors. The value of the thresholds determines the minimum size and energy of a fire that can be detected. We expect the thresholds to be improved and replaced using analyses of data from airborne instrumentation flown in the Smoke Cloud and Radiation (SCAR) experiments in the US and Brazil.

### 3.1.2 DESCRIPTION OF THE ALGORITHM

The following procedures emerge from the physics of fire radiation discussed above and the algorithms used with currently available AVHRR and GOES data. The equations are presented for the day algorithm although the threshold values are provided for day and (night).

1. **Cloud detection and scan angle:** The fire information is derived for all land pixels but the presence of clouds is determined using the MODIS cloud mask. For example, thick clouds, with reflectance larger than 0.2 in the 0.66  $\mu\text{m}$  channel will be identified as these clouds may not be transparent to the fire signal. The MODIS cloud product includes an assessment of the 250 m channels for the presence of cloud. A 45° scan angle cut-off is enforced to limit problems associated with fire detection and characterization at extreme view angles.
2. **Atmospheric correction:** The apparent temperatures  $T_4$  and  $T_{11}$ , will be corrected for gaseous absorption, including water vapor absorption at 11  $\mu\text{m}$ . Note that small clouds may reduce the apparent fire temperature at 11  $\mu\text{m}$  and may impact the water vapor correction in that channel.
3. **Background characterization:** The relationship between the apparent temperatures of the examined pixel and its surrounding pixels is established. The surrounding pixels are used to estimate the background temperature (or non-burning temperature) of the fire pixel. This approach assumes that the correlation between the background temperature of the fire pixel and surrounding pixel temperatures decreases with distance from the pixel. An expanding grid centered on the fire pixel is interrogated until a sufficient number of cloud, water or fire free pixels are identified. We require that 25% of the surrounding background pixels be free of energetic fire pixels, i.e. the box is made larger (up to 21 x 21 pixels) until at least 25% of the pixels in the box are not energetic fire pixels. Water and cloud pixels are also excluded.

Energetic fire pixels are eliminated from the analysis of the characteristics of the background to the fires and are identified as those having  $T_{41} = T_4 - T_{11} \geq 20$  K (10 K at night) and  $T_4 > 320$  K (315 K). Excluding these energetic fires, the average background apparent temperature  $T_{11b}$  and its standard deviation  $\sigma_{T_{11b}}$  are calculated. In a similar way  $T_{4b}$  and  $\sigma_{T_{4b}}$  are calculated. The median temperature difference between the 4  $\mu$ m and 11  $\mu$ m apparent temperatures of the background ( $T_{41b}$ ) and the standard deviation ( $\sigma_{T_{41b}}$ ) are calculated.

4. **Fire detection:** All pixels for which  $T_4 < 315$  K (305 K at night) or  $T_{41} < 5$  K (3 K) are not considered as fires. If the standard deviations  $\sigma_{T_{4b}}$  and  $\sigma_{T_{41b}}$  are less than 2 K, then 2 K is used instead. A pixel is defined as a fire pixel (from the remaining fire pixels) if one of the following five combinations of logical conditions (labeled by letters) are met:

$$\begin{array}{ccc} \text{(A)} & \text{(B)} & \\ \{ [(T_4 > T_{4b} + 4 \sigma_{T_{4b}}) \text{ or } T_4 > 320 \text{ K (315 K at night)}] \text{ and} & & \\ [(\sigma_{T_{41}} > \sigma_{T_{41b}} + 4 \sigma_{T_{41b}}) \text{ or } T_{41} > 20 \text{ K (10 K)}] \} \text{ or } \{ T_4 > 360 \text{ K (330 K)} \} & \text{(1)} & \\ \text{(a)} & \text{(b)} & \text{(X)} \end{array}$$

5. **Glint exclusion:** exclude a fire pixel during the day if it corresponds to glint measurements:  $\rho_{0.64} > 0.3$  and  $\rho_{0.86} > 0.3$  (corresponding to 312 K at 4  $\mu$ m) and glint angle  $< 40^\circ$ .

At this point processing is complete for the level 2 MODIS fire product. Some of the level 3 (gridded) fire products require consolidated (rather than individual) fire pixels, however; for these products several additional steps are performed. These are as follows:

6. **Consolidation:** As a result of the triangular response of MODIS, the same fires may be represented by two adjacent pixels in the scan direction. This will be particularly true for strong fires. Approaches are being developed to consolidate the number of fires after initial detection. One statistical approach, which is currently being evaluated, is outlined below and would be implemented for the 10 km gridded fire product. Since the MODIS triangular response affects the fire pixel distribution only in the scan direction and not in the track direction, significant asymmetry in the fire pixel distribution between the scan and track direction can be used as an indication that a consolidation between adjacent fire pixels is needed. The first step is to determine on a grid of 100 x 100 km: the total number of fire pixels,  $N_f$ , the number of pairs or triplets in the scan direction,  $N_s$ , and the number of pairs or triplets in the track direction,  $N_t$ . If for the pairs or triplets  $N_s - N_t > 3$  and  $N_s - N_t > N_f/3$ , then fire consolidation is required. The detected fires are consolidated in the following way: (1) a single pixel fire

detected, no consolidation; (2) two adjacent fire pixels detected along track, combine the MODIS response for the fires into a single fire detection:

$$L_{4c} = L_4 + L_4 - L_{4b} \quad (2)$$

where the radiance is computed from the Planck function,  $L_4 = P(T_4)$ , for pixel and . The radiance is converted to the combined temperature using the inverse Planck function:  $T_{4c} = P^{-1}(L_{4c})$ . The same consolidation is applied at 11  $\mu\text{m}$ .  $L_{4b}$  is the background radiance at 4  $\mu\text{m}$ .

(3)  $N$  adjacent pixels along track detect fires:

$$\begin{aligned} L_{c1} &= L_1 + \frac{1}{2} L_2 \\ L_{ci} &= \frac{1}{2} L_i + \frac{1}{2} L_{i+1} \quad \text{for} \quad 1 < i < N-1 \\ L_{cN} &= L_N + \frac{1}{2} L_{N-1} \end{aligned} \quad (3)$$

The pixel location of the fire is defined by the weighted average of the centers of the pixels, where the weights are the excess radiance at 4  $\mu\text{m}$ .

**7. Total rate of emission of radiative energy from the fire.** The relationship between the emitted energy and the detected temperature difference in the 4  $\mu\text{m}$  channel is approximated by:

$$E_f = 4.34 \cdot 10^{-19} (T_4^8 - T_{4b}^8) \quad (\text{MWatt per pixel}) \quad (4)$$

The average relationship is shown by the solid line in Fig. 12a.

**8. Smoldering or flaming stage:** This part of the fire algorithm is used to estimate if a detected fire is in mainly a flaming or smoldering phase. Figure 12b shows the relationship between the apparent fire temperatures at 11  $\mu\text{m}$  and 4  $\mu\text{m}$  and the fraction of the combustion in the smoldering phase. To distinguish between smoldering and flaming, it is required that:

$$T_{11} > 2 T_{11b}, \quad T_{11} > 2 \text{ K}, \quad \text{and} \quad T_4 > 10 \text{ K}.$$

Otherwise only  $E_f$  is determined from the average relationship between  $T_4$  and  $E_f$ . The relationship between the apparent temperature at 11  $\mu\text{m}$  and at 4  $\mu\text{m}$  is used to distinguish between 3 possible fire phases, namely only smoldering, only flaming and a mixture of both (see Fig. 12b). To eliminate the effect of background temperature, the apparent temperatures at 11  $\mu\text{m}$  and at 4  $\mu\text{m}$  are first scaled to a background temperature of 300 K and zero reflectance, by subtracting the excess radiance. To generate a threshold that can be used to distinguish between smoldering and flaming, we used a simulation of numerous fires with a varying fraction of smoldering to flaming. The average relationship between  $T_{11}$  and  $T_4$  for all the data is:

$$T_{11} = 0.057 T_4^{1.1} \quad (5)$$

and reflects the change in the fire energy. In Fig. 13 the residue signal at 11  $\mu\text{m}$ :

$T_{11} = T_{11} / (0.057 T_4^{1.1})$  is plotted as a function of  $T_4$ . The residue separates between smoldering flaming and a mixed zone in between. The thresholds that separate between smoldering and flaming are derived from:

If  $T_{11} < 1.0 \text{ K}$  - flaming stage

If  $T_{11} > 1.7 \text{ K}$  - then smoldering stage

Otherwise - a mixed stage

### Fire Products at Coarser Grids

The Level 3 fire products will be generated from all the individual observations stored over a 24 hour period at a Level 2 grid. The Level 2 data base will be archived and made available to the user community. The fire products will be assembled for individual days and summarised for compositing periods of eight days and one month. Products will be available at full resolution (1km) as well as for coarser grids at 10 km and 0.5 degree. These latter products are being designed for use in regional and global modelling.

The information to be stored will include summaries of the actual measured quantities:  $T_4$ ,  $T_{11}$ ,  $T_{4b}$ ,  $T_{11b}$ ,  $T_{4b}$ ,  $T_{11b}$ , total emitted energy,  $E_f$  and flaming/smoldering phase. Statistics on cloud obscured observations will also be stored.

The information for a grid box of 10x10 km and  $0.5^\circ \times 0.5^\circ$ , will classify the fires based on their temperature at 4  $\mu\text{m}$ ,  $T_4$ , (which is proportional to the thermal energy) and store the number of fires identified in each class:

Class 0:  $T_4 < 315 \text{ K}$

Class 1:  $315 \text{ K} < T_4 < 320 \text{ K}$

Class 2:  $320 \text{ K} < T_4 < 325 \text{ K}$

Class 3:  $325 \text{ K} < T_4 < 335 \text{ K}$

Class 4:  $335 \text{ K} < T_4 < 350 \text{ K}$

Class 5:  $350 \text{ K} < T_4 < 400 \text{ K}$

Class 6:  $400 \text{ K} < T_4 < 450 \text{ K}$

Class 7:  $450 \text{ K} < T_4 < 500 \text{ K}$

For each class the average value of  $T_{41} = T_4 - T_{11}$  will also be stored as well as the total thermal energy emitted in the grid box and the average smoldering/total, weighted by the total emitted energy.

Current plans are to provide a MODIS burned area product on a 1 km grid on an 8 day and monthly basis. The product is aimed at meeting the needs of researchers developing emission inventories. The algorithm is currently under development, and comparisons are being made between the use of vegetation indices,

surface reflectance, surface temperature, and surface texture time series. Emphasis is being given to the reflectance component of  $T_4$  at 1 km, which shows a marked contrast between burn scars and surrounding unburned areas (Roy et al. 1998).

### 3.1.3. VARIANCE AND UNCERTAINTIES

The uncertainty in the fire detection and the inversion of the MODIS data into emitted energy and the smoldering/flaming ratio depends on the criteria used for the definition of the fire. The algorithm described in the previous section defines the minimum radiative effects of a fire to be detected by MODIS. The presence of several fire regimes in the pixel defines the meaning of the effective temperature that is derived from the algorithm. These points were discussed in the previous section. In the following we shall present first results of selected sensitivity studies.

Simulations are used to show the sensitivity, expected accuracy and application of the MODIS fire algorithms to synthetic data. The first example given, is a simple simulation of a mixture of smoldering, flaming and background surfaces. Several flaming and smoldering temperatures are used in the simulation, due to the uncertainty in these temperatures: smoldering -  $600\text{ K} \pm 100\text{ K}$  and flaming -  $1000\text{ K} \pm 200\text{ K}$ . The simulation, shown in Fig. 14, is designed to test the possibility of distinguishing between smoldering and flaming conditions from space observations of the spectral apparent fire temperature. The simulation looks for all the possible fire characteristics at the range of temperatures described above, that give the same spectral response at the 4 and 11  $\mu\text{m}$  channels at the satellite sensor. For example, the open circles in Fig. 14, represent fraction of the fire in the smoldering stage between 0 and 40%, and all of them give the same spectral response at 4 and 11  $\mu\text{m}$  of  $T_4 = 400\text{ K}$  and  $T_{11} = 309\text{ K}$ . The simulation shows that the total emitted thermal energy can be much more accurately derived from the measurements than the ratio of the thermal energy emitted in the smoldering or flaming stages. The total emitted energy, that corresponds to a given set of measurements varies by only  $\pm 10\%$ . The ratio of the energy emitted as smoldering to the total, varies usually by  $\pm 20\%$ , which is sufficiently only to distinguish between three stages of fire: flaming, smoldering or mixed stage. Uncertainty in the assumed temperature of the smoldering and flaming stages are the main sources of uncertainty in the derived fire thermal energy and fractionation between smoldering and flaming components.

An additional source of uncertainty is the background characterization. It is possible that the background temperature to the fire that is found within the MODIS fire pixel is different from the background that MODIS senses outside of the MODIS pixel. This can happen, for example, if part of the MODIS pixel is already on fire before the MODIS pass and still has a warmer temperature and higher or lower reflectance at 4  $\mu\text{m}$ . For the strongest fire in Fig. 14 with  $E_f = 1300\text{ Mwatt}$ , an uncertainty in the background temperature of 5 K corresponds to an error in  $E_f$  of only 2% and in the fraction of energy released in the smoldering stage of 5%. Similar errors result from

uncertainty in the surface reflectance at  $4\ \mu\text{m}$  of  $\rho_4=0.05$  for this fire. For fires that consume less biomass and radiate less energy it is more difficult to determine the total emitted energy and fraction of energy emitted in smoldering. For the second smallest fire in Fig. 14, with  $E_f = 230\ \text{Mwatt}$ , the apparent temperature of the fire pixel at  $11\ \mu\text{m}$  is only 9 K more than the background. In this case if the background temperature is underestimated by 5 K, the energy of the fire will be overestimated by 15% and instead of considered as pure flaming, the fire is considered as mixed phase. For the weakest fire in Fig. 12, smoldering or flaming cannot be determined in the presence of such uncertainties in the background temperature or reflectance, but the error in total energy is only 15% for an error in background temperature of 5 K. Therefore it is concluded that uncertainties in the background reflectance and temperature can be tolerated in the derivation of the fire emitted energy but it is possible to distinguish between smoldering and flaming only if the response of the temperature at  $11\ \mu\text{m}$ ,  $T_{11}$ , is at least twice as large as the uncertainty in the background temperature.

The second simulation addresses the large spatial heterogeneity of fires. Each fire pixel was subdivided into 500 zones. The temperature of these zones is defined by 3 main temperatures: background,  $T_b$ , smoldering,  $T_s$ , and flaming,  $T_f$ , but each zone is assigned randomly a temperature in a Gaussian distribution around one of these three temperatures, with a fixed predetermined fraction of smoldering and flaming in the fire pixel. By varying the values of  $T_b$  within 280-320 K,  $T_s$  within 400-600 and  $T_f$  within 700-1300, and varying the width of the distributions, we obtain a variety of conditions that simulate the natural variability. The simulation was performed using Excel with Macro programming for 150 fire pixels, each with a different average temperature and coverage of the smoldering and flaming fires. For each pixel the "true" fire energy was calculated by summing the excess energy in the 500 sub-units. The total radiometric response at  $4\ \mu\text{m}$  and  $11\ \mu\text{m}$  was also calculated and used in the empirical eq. 4 to calculate the apparent fire thermal energy. Fig. 15 shows a comparison between the true and retrieved apparent fire energy. The retrieved fire energy fits the true energy very well. The average standard deviation in deriving the fire energy is 16%. It is larger for small fires and smaller for energetic fires (see Table 6). Inclusion of an uncertainty in surface reflectivity of sunlight between the background and the fire pixel, generated negligible errors in the derived energy for energies larger than 100 MWatt. The error was larger for smaller fires. Table 6. summarizes the results.

*Table 6: Summary of simulation of retrieving the fire thermal energy in the presence of heterogeneity of the fire temperature. 150 fire pixels were simulated with varying fraction of moldering and flaming and varying temperatures. Each fire pixel was divided into 500 zones with temperature chosen randomly in a Gaussian distribution around the flaming, smoldering or background temperatures.*

range of fire energy (MWatt)	average energy for the range (MWatt)	relative error (%) with surface reflectance back=0.1, fire=0.05,	relative error with no surface reflectance
12-1200	218	16	17
12-50	29	38	37
50-100	73	16	19
100-200	142	12	13
200-500	290	9	9
500-1200	643	7	7

### 3.2 PRACTICAL CONSIDERATIONS

This algorithm was implemented as V2.1 code in early 1998 as required for at-launch implementation. During the remaining time to launch, the science team will be pursuing refinement of the algorithm and further developmental work. The revised algorithm will be developed in parallel and will be implemented following evaluation of c. 3 months of global MODIS data. This first major algorithm revision will possibly occur between 6 and 9 months after launch.

#### 3.2.1 PROGRAMMING / PROCEDURAL CONSIDERATIONS

Both the Beta, Version 1, Version 2, and Version 2.1 codes have been delivered to the SDST. The code includes a series of switches which allow a full interrogation of the product inputs and outputs at the SCF.

#### 3.2.2. CALIBRATION and VALIDATION

Calibration of the fire channel is problematic. Although there are plans for calibration of the channel before launch, there are no provisions for on-board calibration after launch above the maximum temperature of the non-fire channel of 335 K and vicarious calibration of the channel will be difficult. Two approaches to vicarious calibration are planned 1) night observation for a large areas with a high temperature (e.g. wide area lava flow). In this case calculation of the warm area size and temperature range using the visible channels (that are calibrated) may be used to compute the expected emission in the 3.95  $\mu\text{m}$  and 11  $\mu\text{m}$  channels. A complex distribution of the temperatures in the pixel may generate an error in the calibration. 2) static gas flares with known emissions. A detailed study of this problem is planned.

Validation of the fire products will be undertaken using a number of independent sources of information. Experience with the AVHRR has shown that it is difficult to validate coarse resolution fire products using ground data. Problems

associated with quantifying the fire temperature and size at the time of overpass indicate the need for remote methods.

Fire temperature and size can be best quantified with higher resolution sensors preferably flying at low altitudes. Airborne instruments such as the MODIS Airborne Simulator (MAS) will provide important data to validate the MODIS Fire Products. Pre-launch airborne campaigns are being implemented to provide data for fire algorithm development and testing (see Section 3.1). The current series of SCAR campaigns is providing important MAS data for this purpose. Targets of opportunity will be explored as part of planned post launch airborne campaigns currently being coordinated through the EOS Validation Office.

NASA intensive field programs such as that planned for Brazil in 1998 (LBA) and the MODIS in Southern Africa Validation Experiment for EOS (SAVE - EOS) in 1999 will provide an important opportunity for fire product evaluation and cost sharing for aircraft overflights. These campaigns will include aircraft missions using the MAS and ground measurement programs to assess the products of biomass burning. The LBA campaign will include analysis of land use fires associated with tropical rain forest conversion. The Southern Africa 1999 campaign will provide a transect from semi-arid to humid savannas. The transect is based on IGBP Kalahari and Miombo regional initiatives. Fires are a common phenomena along all but the most semi arid part of the Transect. Similar campaigns will be needed in temperate and boreal ecosystems during the life of MODIS. Level 3 and 4 EOS Test Sites which are located in fire prone systems will be used as a focus for data collection.

Comparison of fire data from other satellite systems will provide an independent assessment of regional fire distributions as a function of season. The geostationary satellites can provide an assessment of how the MODIS will sample the diurnal cycle of fire activity as a function of biome. GOES-I possesses greater radiometric sensitivity, higher spatial resolution, and improved earth location to within 4 km at the subsatellite point. The five channel images provides diurnal half-hourly 1 km resolution visible (.65  $\mu\text{m}$ ) data; 4 km resolution infrared data in the short (3.9  $\mu\text{m}$ ) and long-wave (10.7  $\mu\text{m}$ ) window channels and the 12  $\mu\text{m}$  channel; and 8 km resolution data in the water vapor channel (6.7  $\mu\text{m}$ ) (Savides et al., 1992). The first of the METEOSAT Second Generation (MSG) satellites is scheduled for launch in 1998. The spectral and spatial characteristics of the MSG will offer a major improvement in the ability to monitor burning activities in Europe and Africa from a geosynchronous platform. The current METEOSAT satellite system provides broadband visible data at 2.5 km resolution, and two channels of infrared data (6.5 and 11  $\mu\text{m}$ ) at 5 km resolution. The instrument to be flown on the MSG is the Spinning Enhanced Visible & Infrared Imager (SEVIRI) consisting of a set of imaging and pseudo-sounding channels providing full disk coverage of Europe, Africa and the Atlantic Ocean every 15-30 minutes. Although the exact configuration of the instrument is still being decided, the SEVIRI is scheduled to include six channels which correspond to the AVHRR-3 channels (0.6  $\mu\text{m}$ , .8  $\mu\text{m}$ , 1.6  $\mu\text{m}$ , 3.8  $\mu\text{m}$ , 10.8  $\mu\text{m}$ , 12.0  $\mu\text{m}$ ; two water vapor channels (6.2  $\mu\text{m}$ , 7.1  $\mu\text{m}$ ); the 8.7  $\mu\text{m}$  channel; and a combination of pseudo-sounding channels which may include the 4.5  $\mu\text{m}$ , 9.7  $\mu\text{m}$ , 13.4  $\mu\text{m}$ , and 14  $\mu\text{m}$  spectral bands. These channels will be available at a resolution of 3 km at the subsatellite point. The sensor will also include a broadband High Resolution Visible (HRV) channel with a resolution of 1 km (Jouan et al, 1993). These data make it possible



to utilize a multispectral thresholding scheme similar to that described for GOES-I to monitor biomass burning activities. This will also represent the first time the scientific community has access to high resolution diurnal shortwave (3.8  $\mu\text{m}$ ) infrared window data over Europe and Africa. In addition to geostationary satellites, the coarse resolution polar orbiting NOAA satellites available in 1998 and beyond will provide an additional source for data cross comparison.

High resolution sensors planned as part of EOS will enable assessment of the fire products. ASTER and Landsat 7 will provide information useful for burn scar validation and fire location to assist in the validation of MODIS fire data. Data from the above systems will be built into the detailed plan for the validation for MODIS fire products. Although ASTER does not have the radiometric resolution to determine fire and smoldering temperatures, the high spatial resolution coupled with the available thermal measurements could assist area calculation studies significantly. The instantaneous observation of ASTER will provide a unique contribution to MODIS validation.

#### Summary of Validation Characteristic and Source Data

- MODIS Diurnal Sampling - GOES /MSG
- Fire spatial distribution, minimum detectable fire size, burned area - ASTER, Landsat 7, MAS flights, Ground data collection
- Flaming and Smoldering Ratio - MAS flights

### 3.2.3 QUALITY CONTROL AND DIAGNOSTICS

The MODIS Fire Product QA will be incorporated into the MODLAND QA plan. The QA metadata includes both mandatory and optional fields. The mandatory fields include the land, water mask and cloud mask from Mod #35 and a user oriented flag as to overall quality on a per pixel basis for all detected fires.. The QA data will include information on the quality of the input data as well as the confidence of detection, the uniformity of the background pixels used and the fire pixel (250 m), the triangular response ie. neighbouring across track response. A switch will be included in the Code to be run at the SCF to allow investigation of the input fields and associated outputs.

Building on the experience with current AVHRR, GEOS and DMSP data, the quality control will include sample manual observation of fires in specific regions and times, the logical conditions that were applied for the specific fire detection and the presence or absence of smoke emerging from the pixel. If fires are detected in an area that is known to be fire free and no smoke is identified from any of the fires, the logical criteria use for the identification of the fires will be reevaluated. The manual observation and first order QA analysis will be done at the MODIS Land Data Operational Product Evaluation Facility.

### 3.2.4 EXCEPTION HANDLING

Data dropouts will be carried forward from those detected for the individual channel inputs. Data collected during orbital manouvers will be excluded from the fire product.

### 3.2.6 DATA DEPENDENCIES

#### 3.2.6.1. Production Dependencies

The MODIS active fire products are dependent on the following information:

- MOD35 cloud mask product - 250m /500m /1km (including cirrus detection)
- solar zenith and azimuth angles
- view zenith and azimuth angles
- uncorrected surface reflectance for bands 1 and 2
- channel 21, 22, and 31 radiances
- land-sea mask

The post-launch burned area product will be dependent on at least the following information:

- Level 3 fire product
- vegetation index product at 250 m
- channel 20 radiance
- Previous Fire Record- QA (MODIS derived statistics - AVHRR fire statistics at launch)

#### 3.2.6.2. QA and Validation Data Dependencies

Landsat 7 and ASTER data will be needed for validation. It is anticipated that MODIS Fire team will request between 5-10 high resolution scenes per month during the two years for fire product validation. These requests will be made on demand following preliminary QA and in support of field campaigns. An up-to-date inventory of data acquired from these sensors will be needed to optimize data ordering. It is expected that delivery of data within two weeks of ordering will be adequate to meet these needs.

In the post - launch phase data will be needed from the Geostationary satellites for MODIS validation and quality assessment. Active collaborations will be expanded within the MODIS fire team to provide some intercomparisons and permit evaluation of the MODIS overpass times in terms of the diurnal cycle. MODIS resources will need to be obtained to secure the data necessary for the inter satellite data comparisons.

### 3.2.7 OUTPUT PRODUCTS

3.2.7.1 The MODIS fire products currently consist of the following product suite and associated information:

- Daily Fire Occurrence at 1km

-----

- Daily Fire Occurrence (24 hrs - using day/night algorithm )
- Emitted Energy (for each 2G grid cell, the most energetic fire will be selected from all the orbits and observations collected during the 24 hr period )
- Logical criteria used for the fire selection (day/night)
- Fire pixel values and background values

- Eight Day 1km Composite (Simplified 8-bit Browse Product)

-----

- No of Fires detected
- Number of cloudy days
- Logic of most confident fire detected
- Energy associated with and most energetic fire during the 8 day period

- 10 by 10 km Gridded Statistical Product (daily / 8 day/monthly)

-----

( to be derived from the daily fire occurrence product)

- Number of Fires (consolidated by row and column statistics) by Class 0-7
- Summarized Energy
- Summarized Flaming and Smoldering Ratio

- 50 by 50 km Gridded Statistical Product (daily/ 8 day/ monthly)

presented in the MODIS Land Climate Modelling Grid

-----

( to be derived from the daily fire occurrence product)

- Number of Fires (consolidated by row and column statistics) by Class 0-7
- Summarised Energy
- Summarised Flaming and Smoldering Ratio

- Burned Area (Post Launch) (1 km grid / 8 day / monthly/ annual)

-----

- % Area burned
- Land cover type

### 3.2.7.2 The Volcano /Fire (48hr) Alert Product

The EOS Volcanology Team has developed an algorithm which will detect thermal anomalies (volcanic eruptions, fires, etc.) apparent in the MODIS Level 1B data stream. The purpose of EOS IDS product 3290, Surface Thermal Alert, is to provide a rapid means to qualitatively search for thermal anomalies in the MODIS data stream and to display results at a web-site in as close to real-time as possible. Since the product will also

detect fires, the generated output will also be very useful to compare with the more quantitatively-oriented MODIS Fire Products. The Surface Thermal Alert also be useful for rapid target designation for higher spatial resolution instruments such as ASTER, Landsat 7, and the Hyperspectral Imager.

**Description:** The entire MODIS Level 1B nighttime data stream will be continuously searched during Level 2 production by a portion of the MODIS Fire Algorithm Code executed at the MODIS TLCF in near-real time, using 5 MODIS bands. Data for alerts that are triggered will be sent to the Univ. Hawaii SCF. The alert fields will be viewed using a limited interactive display on a Web-site, which will allow display of regional or global maps showing locations of alerts and indicating type (volcano/non-volcano) and severity by color or gray-scale differences. The spatial resolution will be 1 km.

**Input:** Continuous observation of the MODIS Level 1B nighttime data stream by the MODIS TLCF, conducted as part of a collaborative effort with the MODIS Science Data Support Team and the MODLAND Fire Group. The alert files will be sent directly from the MODIS TLCF to the Univ. of Hawaii SCF, where the classification of alerts will be done. The input for alerts will be Channels 21, 22, 29, 31, and 32.

**Output from the Univ. Hawaii SCF:**

The Surface Thermal Alert will not generate any type of product within the MODIS Fire Algorithm structure. The "output" file of alerts will be transferred to the Univ. of Hawaii SCF for further processing. A copy of the "output" file will not be stored at the DAAC as the other MODIS Fire Products in this ATBD.

Alert files will be approximately 50 bytes per record (HDF binary) containing date, time, latitude, longitude, 5 DN values of alert data, an alert qualifier (volcano/non-volcano, severity), and version number of the nighttime alert software. One MODIS global pass per night will yield on the order of 10,000 alerts/night from alerted locations.

**Data Availability:** Alerts of up to 1 week old will be located on a Web-site maintained by the EOS Volcanology IDS Team. Within two days of final processing at the Hawaii SCF, alert data in 24-hour increments, will be moved to an as-yet undesignated site for archiving and possible data-querying.

### 3.3 CONSTRAINTS, LIMITATIONS, ASSUMPTIONS

There are several main assumptions associated with the fire product that will require further study in the pre-launch period:

Assumptions concerning background temperature uniformity.  
Assumptions concerning the prelaunch calibration of the high gain channels.  
Assumptions concerning the accuracy of the MODIS geolocation.  
Assumptions concerning the instrument performance re. the fire bands

The prelaunch calibration of the high gain channels require careful consideration by the MODIS calibration working group.

#### **4.0 An outline of the agenda for product research and development**

##### **4.1 REMAINING PRELAUNCH PRODUCT RESEARCH AND DEVELOPMENT PRIORITIES**

In the remaining period prior to launch it is necessary to refine and evaluate the proposed algorithms for MODIS. This will be done using three primary methods: theoretical simulation, airborne data from the MAS and AVHRR data analyses. The three approaches have different strengths. The MODIS Airborne Simulator offers the best opportunity for simulating the MODIS instrument and campaigns are planned to include fire monitoring. A campaign was undertaken in the Western US (SCAR C) in 1994 and in Brazil (SCAR B) in 1995. In this latter experiment 1000's of fires were observed with the MAS and statistical analyses are currently being undertaken. Preliminary results show an excellent correspondence between the MAS data and our theoretical analysis.

Research areas targeted for attention include: development of product QC, the pre-launch calibration accuracy of the MODIS fire channels, the development of approaches for post-launch vicarious calibration, the spatial characteristics of fire events and their impact on inversion results, the diurnal cycle of fire with respect to the MODIS AM and PM sampling, the evaluation of a prototype 1km AVHRR global fire product for evaluation of seasonal fire distributions, the evaluation of the accuracy of the ancillary data inputs for the fire product, in particular the background temperature, with respect to fire product accuracy. In the prelaunch phase we will be developing the burn scar algorithm and evaluating the flaming to smoldering ratio estimation technique.

##### **4.2 POST LAUNCH DEVELOPMENT ACTIVITIES**

The primary activity post - launch will be the evaluation, validation and refinement of the MODIS fire products. The details of this post launch development activity have yet to be defined, however they will certainly include development of improved multispectral criteria for the daytime algorithms. In the post launch period procedures for estimating burned area from MODIS will be tested.

#### **Acknowledgments.**

The authors wish to thank the contributors to the IGBP-DIS Fire Algorithm Workshop Report ( Cahoon, Dowty, Kasischke, Kendall, Prins). Material from the IGBP report has been reproduced extensively in the first part of this document.

Fig 1. Plot of the spectral two way transmission in the mid-IR (thick solid line) and the location of the two MODIS mid-IR channels (thick black bars). The contribution to the reduction in the transmission from absorption by water vapor (dotted red line),  $N_2$  (dashed black line),  $N_2O$  (dot-dashed green line) and  $CO_2$  (dot-dot-dot-dashed blue line) are shown. While the absorption at  $3.8 \mu m$  is affected mainly by water vapor absorption, the absorption at  $4 \mu m$  is dominated by  $N_2$  absorption.

Fig 2. The MODIS response across track and the definition of the MODIS pixel. A fire in a given location (black bar in the middle of the abscissa) can be observed by two adjacent pixels as indicated by the arrow

Fig. 3: Simulation of the effect of fire heterogeneity on the retrieval of fire thermal energy. A comparison is plotted between the simulated and retrieved fire energy. 150 fire pixels were simulated. Each composed of 500 zones with different temperature but following Gaussian distributions around an average background, smoldering and flaming temperatures. The fraction of smoldering and flaming varies from pixel to pixel. The average temperatures and standard deviations vary too. The simulated fire energy is the sum of the energies in the 500 zones. The retrieved fire energy is retrieved from the average radiance at  $4 \mu m$ . It fits the simulated energy very well. The average standard deviation in deriving the fire energy is 16%. It is larger for small fires and smaller for energetic fires.

Fig. 4: Image of  $210 \text{ km} \times 180 \text{ km}$  of the Yellowstone National Park fire area at  $500 \text{ m/pixel}$  spatial resolution. The image is a false color composite generated using TM data at  $2.2 \mu m$ ,  $1.65 \mu m$ , and  $0.66 \mu m$ , which were resampled to create MODIS corresponding channels 7, 6, and 1. A distance scale marking  $30 \text{ km}$  is located in the lower right part of the image, while a north arrow indicator is in the lower left. In this false color scheme the unburned forest is deep green, large water bodies (for example, Yellowstone Lake denoted by "YL" in the image) are dark blue, and clouds are white. Active fires are bright pink, while recent burn scars ( $< 3$  days old) are brick red. Older burn scars are included in the yellow portions of the image. As a reference point, Old Faithful Visitor Center is indicated with a bright red dot towards the center of the image.

Fig. 5: A  $15 \text{ km} \times 15 \text{ km}$  subarea of Fig. 13 at  $30 \text{ m/pixel}$  spatial resolution. A firestorm passed over the Old Faithful Visitor Center (marked VC) 19 hours before the data were acquired. (a) is a false color of  $11 \mu m$  (red),  $2.2 \mu m$  (green), and  $1.65 \mu m$  (blue) combination which shows the recent burn scars in pink and red, and active fires in yellow-white. (b) is a false color of  $11 \mu m$  (red),  $0.66 \mu m$  (green),  $0.48 \mu m$  (blue) combination which shows the outline of the burn scars (red and white) along with the associated smoke plumes (blue) generated from especially strong fires. White areas have high radiances in all bands which means that they are smoke-covered active fires, burn scars, or natural thermal springs.

Fig. 6: Images of the same area as in Fig. 4, but here the TM data were resampled and rescaled to simulate MODIS channels at 11  $\mu\text{m}$ , 4  $\mu\text{m}$ , and 1.65  $\mu\text{m}$ , which in the image are red, green, and blue, respectively. (a) - 30 m/pixel spatial resolution data, (b) - resampled to the MODIS 1 km data. The white/yellow areas represent relatively high concentrations of active fires (high radiances in all bands), while the reddish-pink areas are either burn scars or natural thermal springs and mud pots. The two primary fire areas shown in this image advanced from the lower left corner of the image (SW) towards the upper right corner of the image (NE).

Fig. 7: Comparison of the energy calculated in two ways from a single data set, corresponding to Fig. 5. The first method (x-axis) is to calculate the energy of each 30 m pixel and then resampled to 1km/pixel spatial resolution, while the second method (y-axis) is to calculate the energy by resampling the 30 m radiances to 1 km spatial resolution, and then converting to energy. (a) - results for a straight average resulting in 196 (14 x 14) rectangular pixels, (b) - results for the MODIS triangular conversion. Clusters of points near 500 W/m<sup>2</sup> represent the pixels radiating at background temperatures (303 K). Contrary to intuition, the produced curve does not exactly match a line having a slope of 45°. Rather it is slightly bowed upwards, showing that for identical fire areas, averaging radiances to 1 km first and then calculating energies (i.e., the MODIS instrument) will result in higher energy values than those obtained from higher spatial resolution data.

Fig 8: Observations of fire and smoke from the MAS imagery for the Quinault fire for the first pass of the ER-2 above the fire. On the right is a MAS false color image showing the shore line and the fire and smoke at 19:12 GMT. The fire zone is expanded into the image in the left top and the calculations of the thermal energy emitted from the fire is shown in the bottom left.

Fig. 9: Relationship between the rate of emission of thermal radiative energy from the Quinault fire and the rate of emission of smoke particulates from the fire. The thermal radiation is computed from MAS observations at 1.6  $\mu\text{m}$  assuming that each pixel is a black body. The rate of emission of smoke particulates is derived from MAS observations of the smoke over the water downwind from the fire at 0.66  $\mu\text{m}$ . The results are compared with the size of the fire detected by MAS at 4  $\mu\text{m}$  and the model predictions of the Forest Service for the heat release and for the total particulate mass for size under 2.5  $\mu\text{m}$ . The model is based on ground based observations of the fuel load, ignition and consumption. Note the strong similarity between the time dependence of the rate of emission of radiative energy, the fire size and the rate of emission of smoke as obtained from the remote sensing data.

Fig. 10: The sensitivity of the MODIS channels to the fraction of the pixel covered by flames of 1000K ( $f_{\text{flame}}$ ), and fraction of the pixel covered by smoldering of 600K. The rest of the pixel is assumed to have a temperature of 300K.

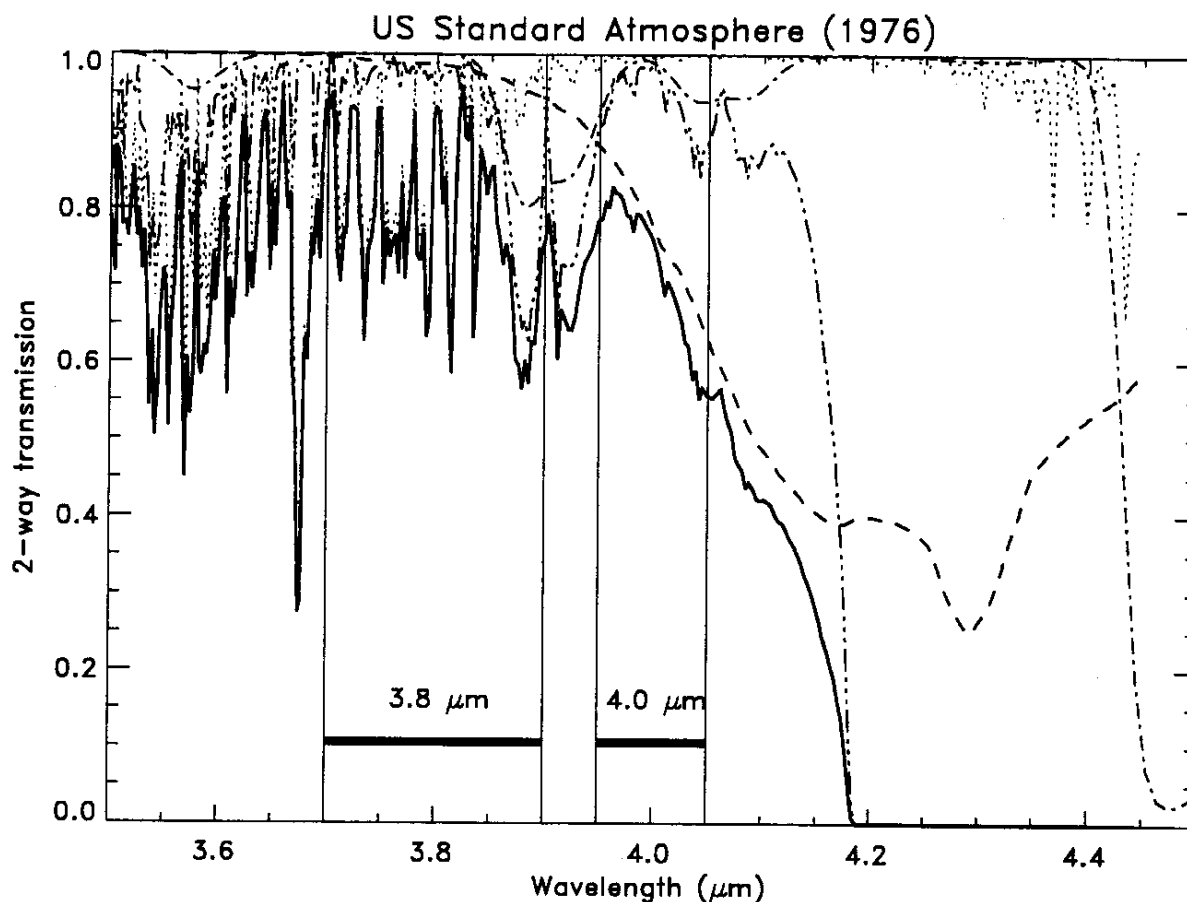


Fig. 11: The apparent temperature of the pixel at 4  $\mu\text{m}$ , as observed by MODIS, as a function of the fraction of the pixel covered by the fire and its temperature.

Fig. 12: Relationship between the total energy emitted from the fire  $E_f$  ( $E_{\text{total}}$ ), the apparent temperature of the pixel at 11  $\mu\text{m}$  and the apparent temperature at 4  $\mu\text{m}$  ( $T_4$ ).  $E_f$  can be computed from  $T_4$  using the solid line approximation in (a) given by  $E_f = 4.34 \cdot 10^{-19} (T_4^8 - T_{4b}^8)$ , where  $T_{4b}$  is the background apparent temperature. The figure is constructed from a compilation of values for thousands of fire scenarios defined by the temperature of the smoldering phase, the temperature of the flaming phase and the fraction of the 1  $\text{km}^2$  pixel that is occupied by each of them.  $T_{11}$  is also sensitive to the ratio of smoldering/flaming and can be used to derive it.

Fig. 13 Residue signal at 11  $\mu\text{m}$  that is used to differentiate between smoldering and flaming:  $T_{11} = T_{11} / (0.0057 T_4^{1.1})$ , plotted as a function of the fire signal at 4  $\mu\text{m}$ ,  $T_4$ . The thresholds of  $T_{11}$  that separate between smoldering and flaming are:

If  $T_{11} < 1.0\text{K}$  then flaming stage  
 If  $T_{11} > 1.7\text{K}$  then smoldering stage  
 Otherwise: a mixed stage



solid line = total transmission  
 dotted line = H<sub>2</sub>O vapor transmission  
 dashed line = N<sub>2</sub> transmission  
 dot-dashed line = N<sub>2</sub>O transmission  
 dot-dot-dot-dashed line = CO<sub>2</sub> transmission

**Fig 1.** Plot of the spectral two way transmission in the mid-IR (thick solid line) and the location of the two MODIS mid-IR channels (thick black bars). The contribution to the reduction in the transmission from absorption by water vapor (dotted red line), N<sub>2</sub> (dashed black line), N<sub>2</sub>O (dot-dashed green line) and CO<sub>2</sub> (dot-dot-dot-dashed blue line) are shown. While the absorption at 3.8 is affected mainly by water vapor absorption, the absorption at 4  $\mu\text{m}$  is dominated by N<sub>2</sub> absorption.

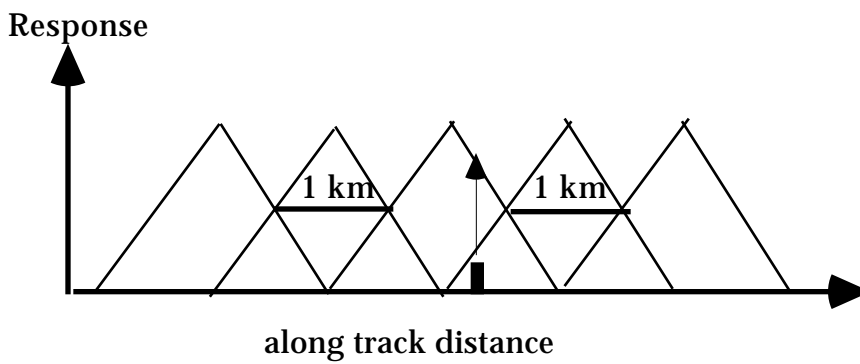


**Fig. 2:** The MODIS response across track and the definition of the MODIS pixel. A fire in a given location (black bar in the middle of the abscissa) is usually observed by two adjacent pixels as indicated by the arrow

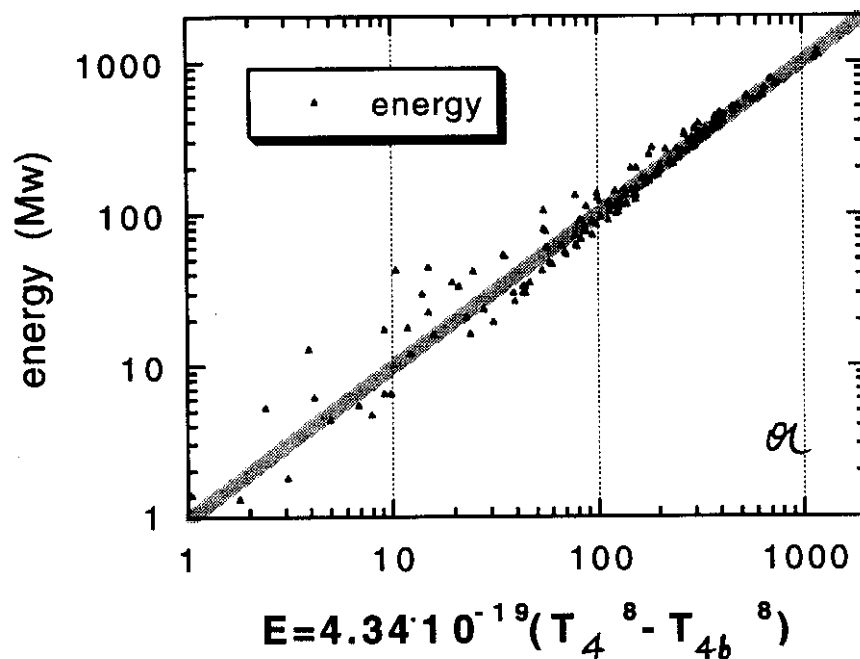


**Fig. 3:** Simulation of the effect of fire heterogeneity on the retrieval of fire thermal energy. A comparison is plotted between the simulated and retrieved fire energy. 150 fire pixels were simulated. Each composed of 500 zones with different temperature but following Gaussian distributions around an average background, smoldering and flaming temperatures. The fraction of smoldering and flaming varies from pixel to pixel. The average temperatures and standard deviations vary too. The simulated fire energy is the sum of the energies in the 500 zones. The retrieved fire energy is retrieved from the average radiance at 4  $\mu\text{m}$ . It fits the simulated energy very well. The average standard deviation in deriving the fire energy is 16%. It is larger for small fires and smaller for energetic fires.

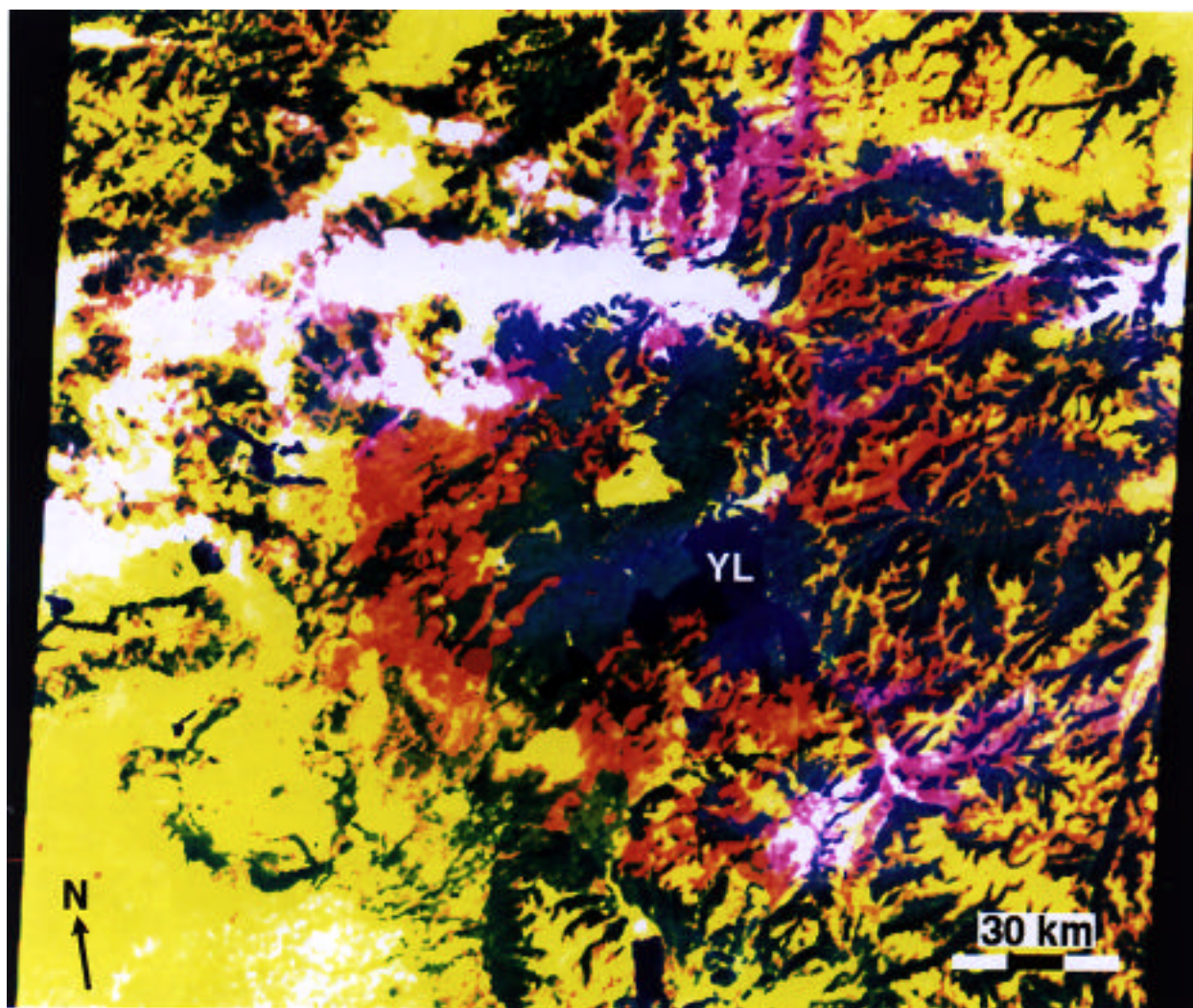


**Fig. 4:** Image of 210 km x 180 km of the Yellowstone National Park fire area at 500 m/pixel spatial resolution. The image is a false color composite generated using TM data at 2.2  $\mu\text{m}$ , 1.65 $\mu\text{m}$ , and 0.66  $\mu\text{m}$ , which were resampled to create MODIS corresponding channels 7, 6, and 1. A distance scale marking 30 km is located in the lower right part of the image, while a north arrow indicator is in the lower left. In this false color scheme the unburned forest is deep green, large water bodies (for example, Yellowstone Lake denoted by "YL" in the image) are dark blue, and clouds are white. Active fires are bright pink, while recent burn scars (< 3 days old) are brick red. Older burn scars are included in the yellow portions of the image. As a reference point, Old Faithful Visitor Center is indicated with a bright red dot towards the center of the image.

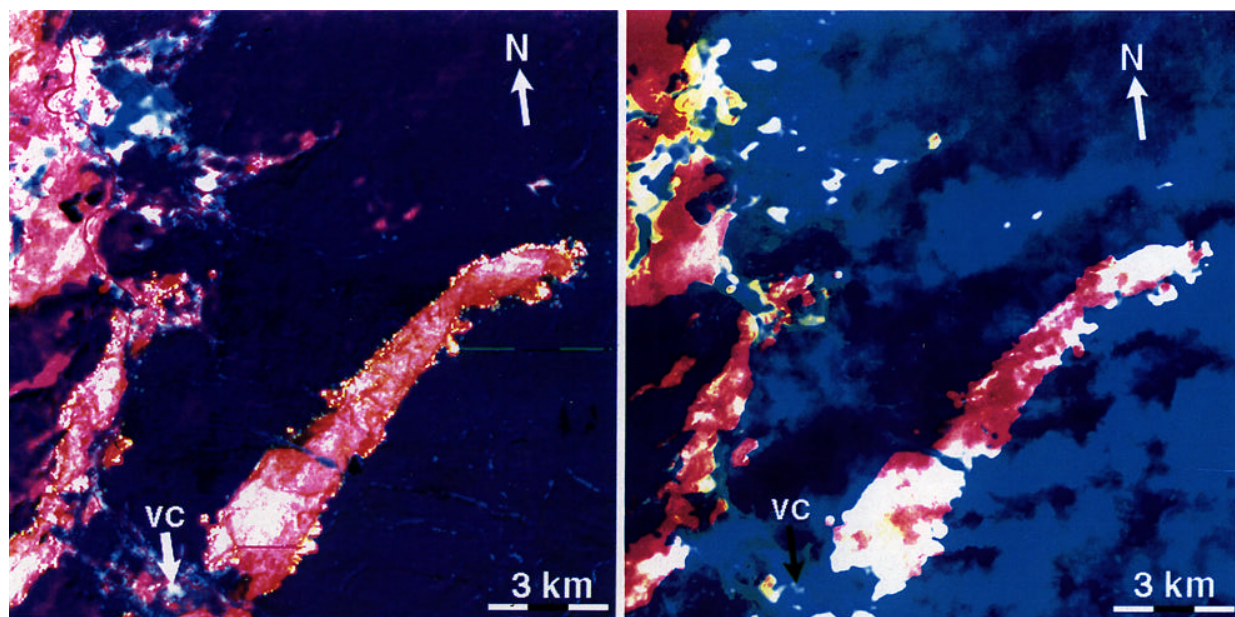


**Fig. 5:** A 15 km x 15 km subarea of Fig. 13 at 30 m/pixel spatial resolution. A firestorm passed over the Old Faithful Visitor Center (marked VC) 19 hours before the data were acquired. (a) is a false color of 11  $\mu\text{m}$  (red), 2.2  $\mu\text{m}$  (green), and 1.65  $\mu\text{m}$  (blue) combination which shows the recent burn scars in pink and red, and active fires in yellow-white. (b) is a false color of 11  $\mu\text{m}$  (red), 0.66  $\mu\text{m}$  (green), 0.48  $\mu\text{m}$  (blue) combination which shows the outline of the burn scars (red and white) along with the associated smoke plumes (blue) generated from especially strong fires. White areas have high radiances in all bands which means that they are smoke-covered active fires, burn scars, or natural thermal springs.



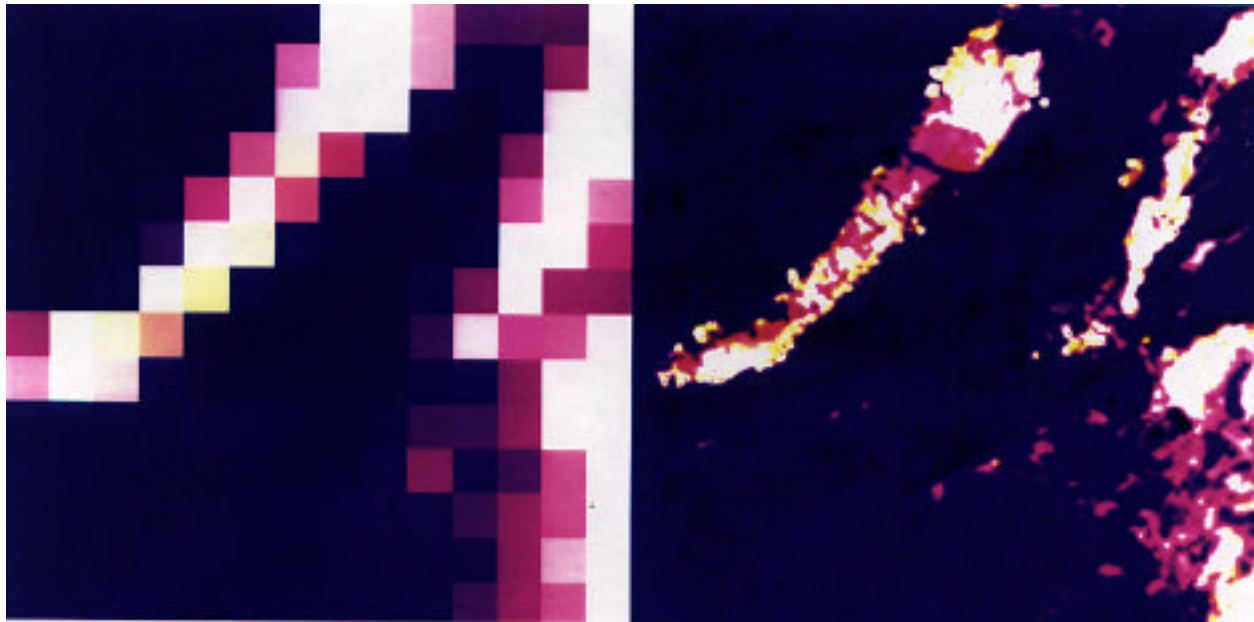


**Fig. 6:** Images of the same area as in Fig. 4, but here the TM data were resampled and rescaled to simulate MODIS channels at 11  $\mu\text{m}$ , 4  $\mu\text{m}$ , and 1.65  $\mu\text{m}$ , which in the image are red, green, and blue, respectively. (a) resampled to the MODIS 1 km data (b) 30m/pixel spatial resolution data. The white/yellow areas represent relatively high concentrations of active fires (high radiances in all bands), while the reddish-pink areas are either burn scars or natural thermal springs and mud pots. The two primary fire areas shown in this image advanced from the lower left corner of the image (SW) towards the upper right corner of the image (NE).

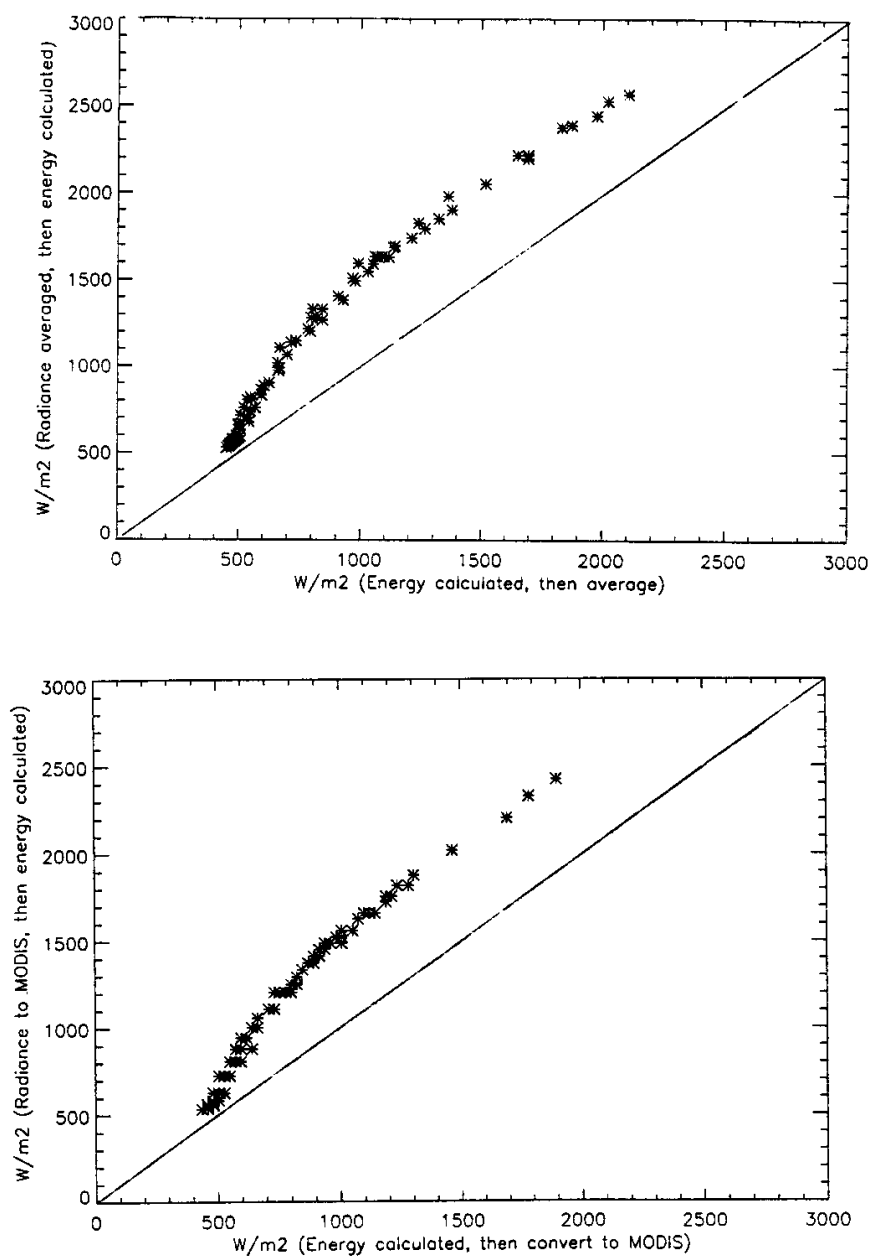


**Fig. 7:** Comparison of the energy calculated in two ways from a single data set, corresponding to Fig. 5. The first method (x-axis) is to calculate the energy of each 30 m pixel and then resampled to 1km/pixel spatial resolution, while the second method (y-axis) is to calculate the energy by resampling the 30 m radiances to 1 km spatial resolution, and then converting to energy. (a) - results for a straight average resulting in 196 (14 x 14) rectangular pixels, (b) - results for the MODIS triangular conversion.



Clusters of points near  $500 \text{ W/m}^2$  represent the pixels radiating at background temperatures (303 K). Contrary to intuition, the produced curve does not exactly match a line having a slope of  $45^\circ$ . Rather it is slightly bowed upwards, showing that for identical fire areas, averaging radiances to 1 km first and then calculating energies (i.e., the MODIS instrument) will result in higher energy values than those obtained from higher spatial resolution data.



**Fig 8:** Observations of fire and smoke from the MAS imagery for the Quinault fire for the first pass of the ER-2 above the fire. On the right is a MAS false color image showing the shore line and the fire and smoke at 19:12 GMT. The fire zone is expanded into the image in the left top and the calculations of the thermal energy emitted from the fire is shown in the bottom left.

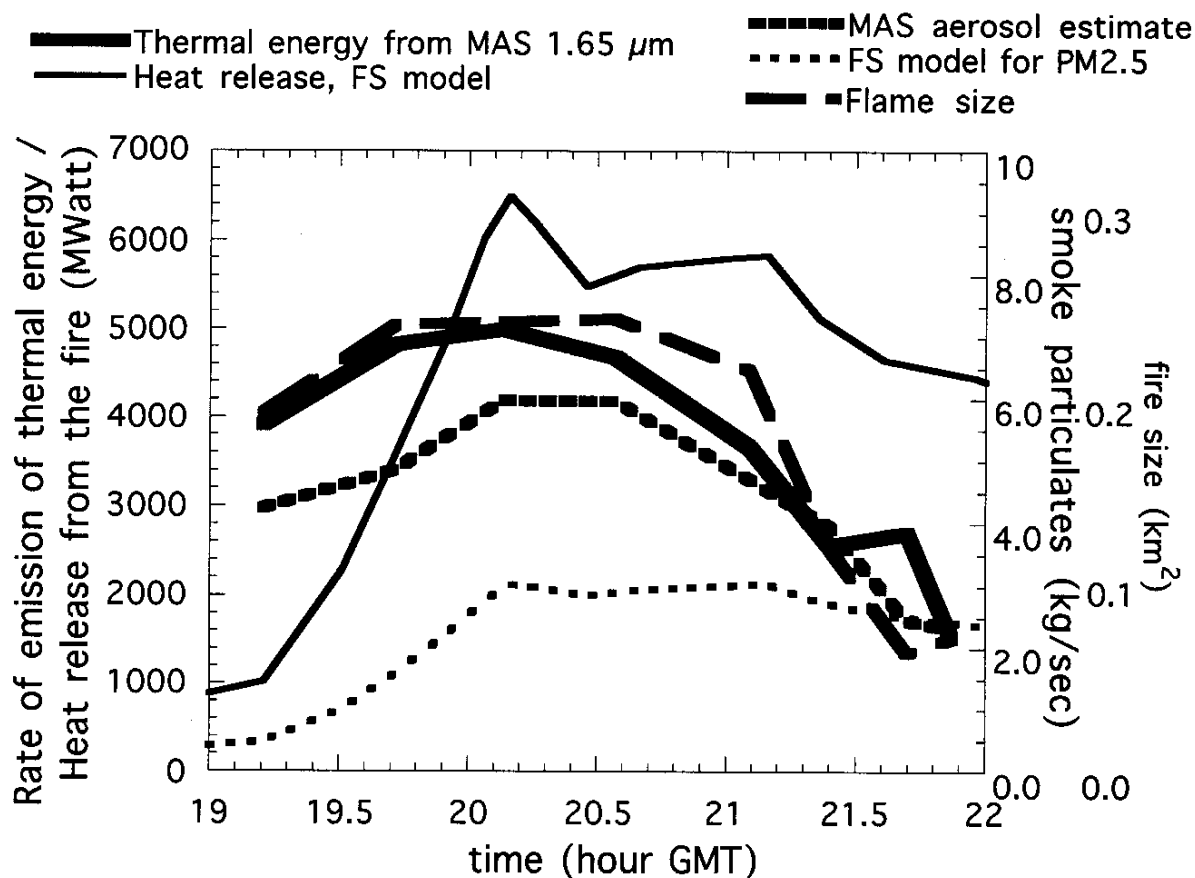


**Fig. 9:** Relationship between the rate of emission of thermal radiative energy from the Quinault fire and the rate of emission of smoke particulates from the fire. The thermal radiation is computed from MAS observations at 1.6  $\mu\text{m}$  assuming that each pixel is a black body. The rate of emission of smoke particulates is derived from MAS observations of the smoke over the water downwind from the fire at 0.66  $\mu\text{m}$ . The results are compared with the size of the fire detected by MAS at 4  $\mu\text{m}$  and the model predictions of the Forest Service for the heat release and for the total particulate mass for size under 2.5  $\mu\text{m}$ . The model is based on ground based observations of the fuel load, ignition and consumption. Note the strong similarity between the time dependence of the rate of emission of radiative energy, the fire size and the rate of emission of smoke as obtained from the remote sensing data.

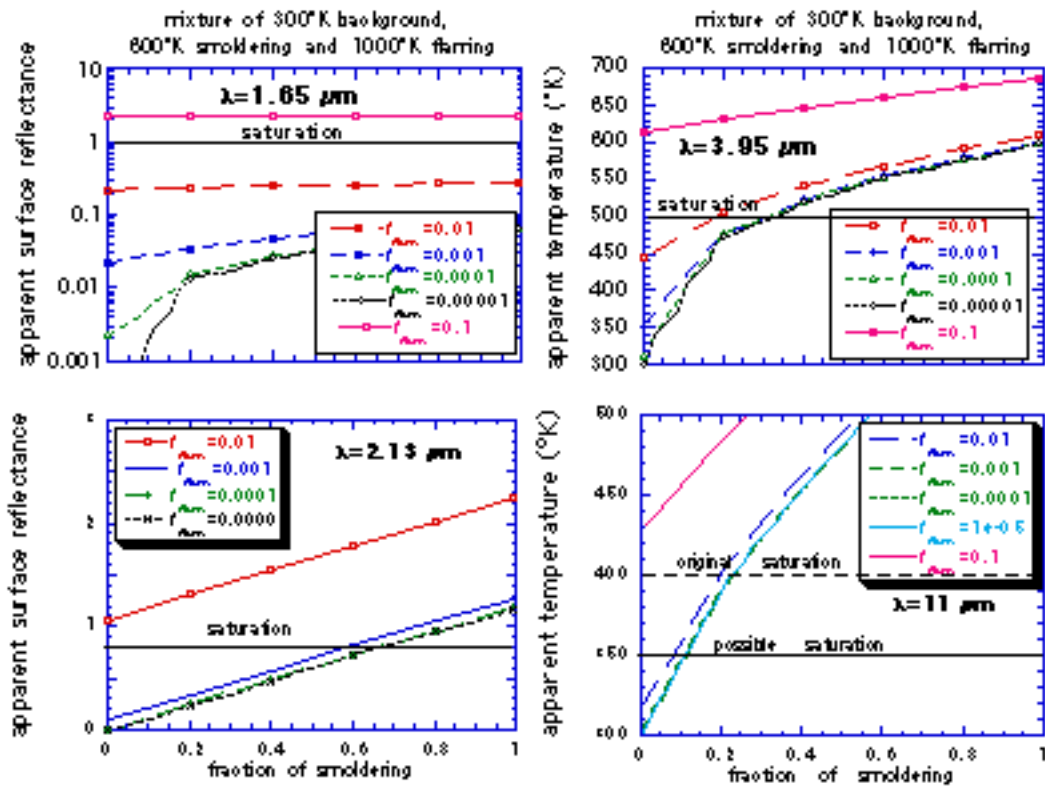


**Fig. 10:** The sensitivity of the MODIS channels to the fraction of the pixel covered by flames of 1000K ( $f_{\text{flame}}$ ), and fraction of the pixel covered by smoldering of 600K. The rest of the pixel is assumed to have a temperature of 300K.

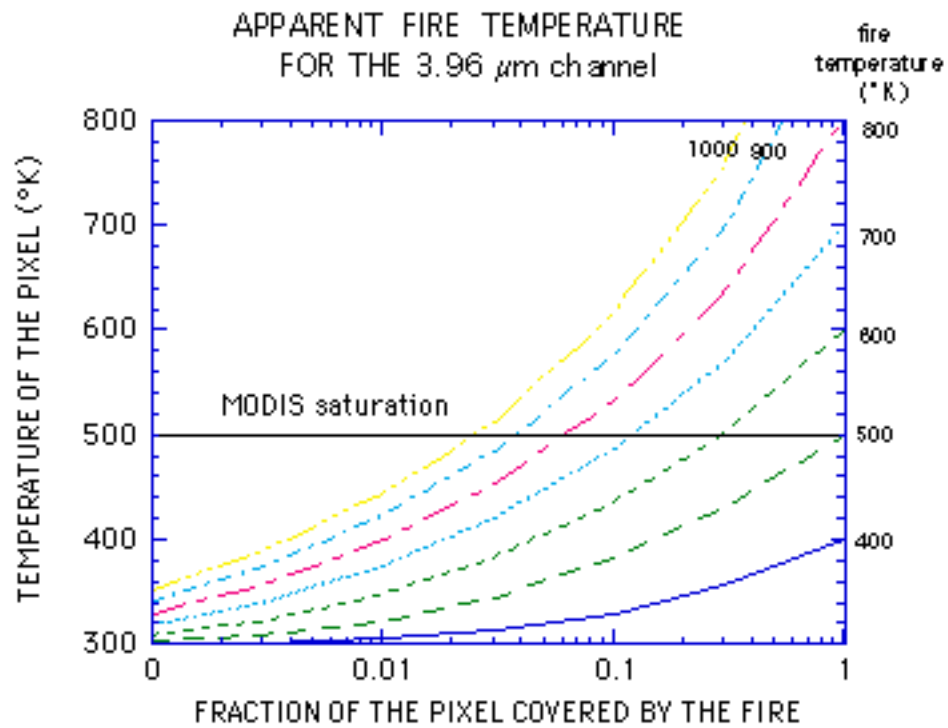


**Fig. 11:** The apparent temperature of the pixel at 4  $\mu\text{m}$ , as observed by MODIS, as a function of the fraction of the pixel covered by the fire and its temperature.

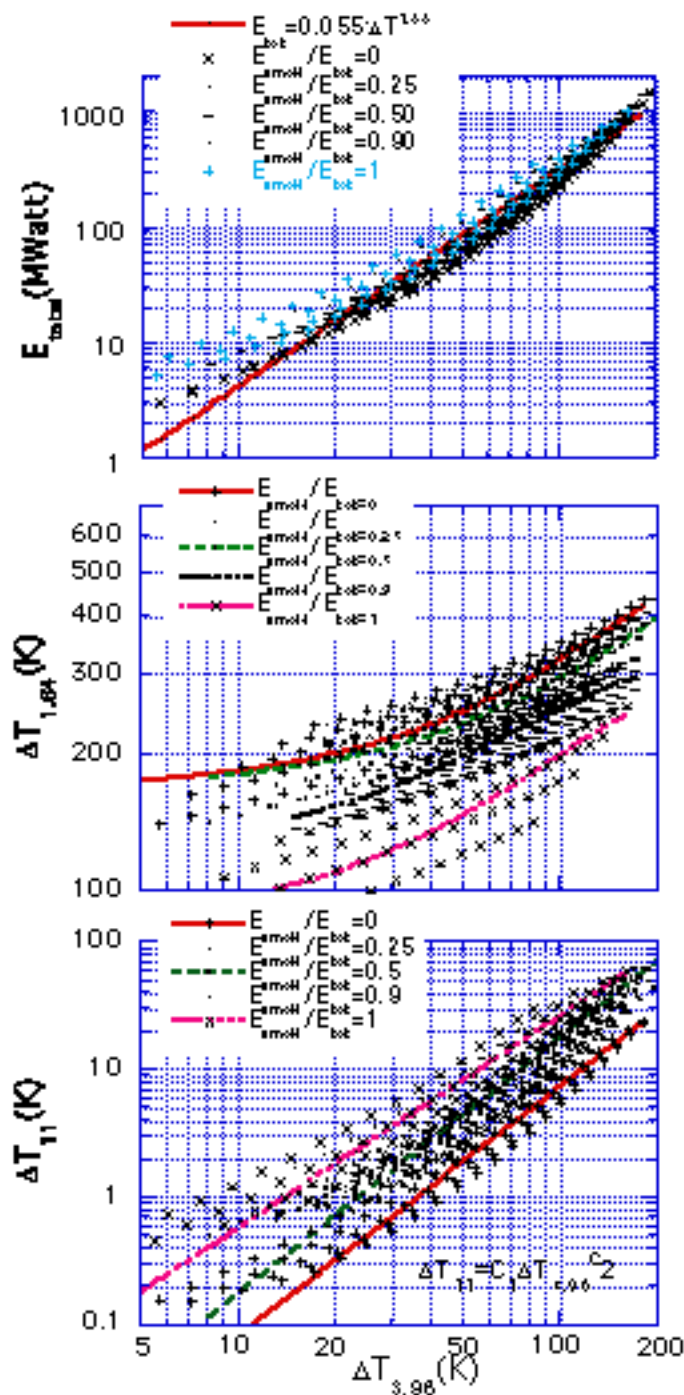


**Fig. 12:** Relationship between the total energy emitted from the fire  $E_f$  ( $E_{total}$ ), the apparent temperature of the pixel at 11  $\mu m$  and the apparent temperature at 4  $\mu m$  ( $T_4$ ).  $E_f$  can be computed from  $T_4$  using the solid line approximation in (a) given by

$E_f = 4.34 \cdot 10^{-19} (T_4^8 - T_{4b}^8)$ , where  $T_{4b}$  is the background apparent temperature. The figure is constructed from a compilation of values for thousands of fire scenarios defined by the temperature of the smoldering phase, the temperature of the flaming phase and the fraction of the 1 km<sup>2</sup> pixel that is occupied by each of them.  $T_{11}$  is also sensitive to the ratio of smoldering/flaming and can be used to derive it.

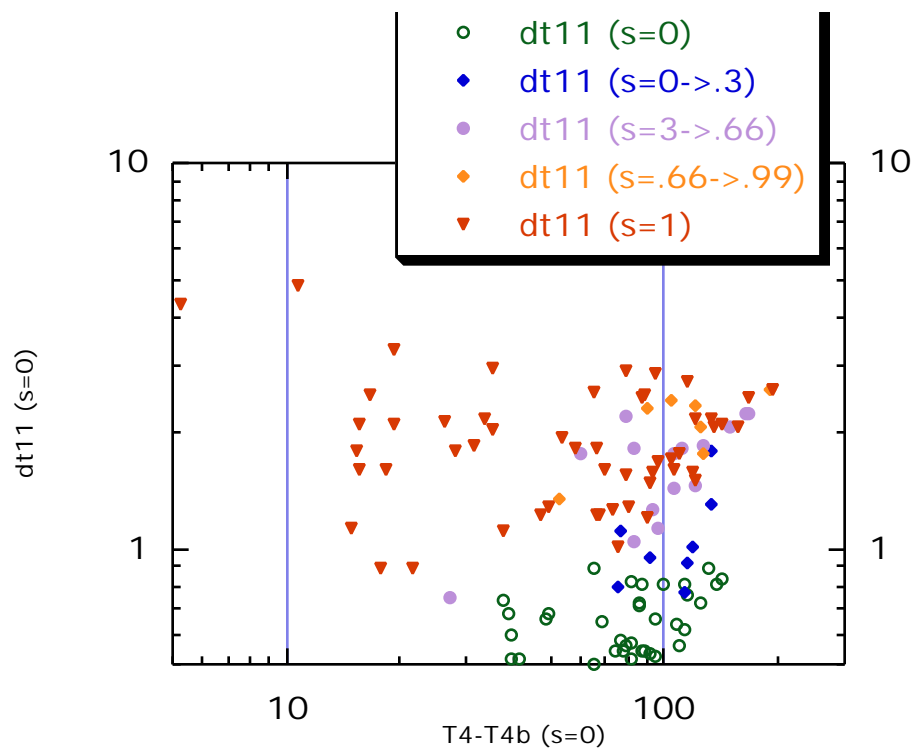


**Fig. 13** Residue signal at 11  $\mu\text{m}$  that is used to differentiate between smoldering and flaming:  $T_{11} = T_{11} / (0.0057 T_4^{1.1})$ , plotted as a function of the fire signal at 4  $\mu\text{m}$ ,  $T_4$ . The thresholds of  $T_{11}$  that separate between smoldering and flaming are:

If  $T_{11} < 1.0K$  then flaming stage  
 If  $T_{11} > 1.7K$  then smoldering stage  
 Otherwise: a mixed stage



**REFERENCES**

- Andreae, M.O., E.V. Browell, M. Garstang, G.L. Gregory, R.C. Harriss, G.F. Hill, D.J. Jacob, M.C. Pereira, G.W. Sachse, A.W. Setzer, P.L. Silva Dias, R.W. Talbot, A.L. Torres, S.C. Wofsy, 1988, Biomass-burning and associated haze layers over Amazonia, Journal of Geophysical Research, 93:1509-1527.
- Andreae, M. O., 1991: Biomass burning: its history, use, and distribution and its impact on environmental quality and global climate. In: Global Biomass Burning, p. 3-21, J. S. Levine(Ed.). Cambridge, MA: The MIT Press.
- Belward, A.S., P.J. Kennedy and J-M. Gregoire, 1993, The limitations and potential of AVHRR GAC data for continental scale fire studies, Int. J. Remote Sensing.
- Browell, E. V., G. L. Gregory and R.C. Harriss, 1988: Tropospheric ozone and aerosol distributions across the Amazon Basin. J. Geophysical Res., 93, 1431-1451.
- Brustet, Jean Michel, Jean Bruno Vickos, Jacques Fontan, Katherine Manissadjian, Alain Podaire, and François Lavenue, 1991a, Remote Sensing of Biomass Burning in West Africa with NOAA-AVHRR, In: Global Biomass Burning, Joel S. Levine (ed.), The MIT Press, Cambridge, Massachusetts, pp.47-52.
- Cahoon, Donald R., Jr., Joel S. Levine, Wesley R., Cofer III, James E. Miller, Patrick Minnis, Geoffrey M. Tennille, Tommy W. Yip, Brian J. Stocks, and Patrick W. Heck, 1991, The Great Chinese Fire of 1987: A View from Space, In: Global Biomass Burning, Joel S. Levine (ed.), The MIT Press, Cambridge, Massachusetts, pp.61-66.
- Cahoon, D.R. Jr., Brian J. Stocks, Joel S. Levine, Wesley R. Cofer III and Charles C. Chung, 1992a, Evaluation of a Technique for Satellite-Derived Area Estimation of Forest Fires, Journal of Geophysical Research, 97(D4):3805-3814.
- Cahoon, D.R. Jr., B.J. Stocks, J.S. Levine, W.R. III Cofer and K.P. O'Neill, 1992b, Seasonal distribution of African savanna fires, Nature, 359:813-815.
- Charlson, R. J., J. Langner, H. Rodhe, C.B. Leovy and S.G. Warren, 1991: Perturbation of the northern hemisphere radiative balance by backscattering from anthropogenic sulfate aerosols. Tellus, 43AB, 152-163.
- Coakley, J.A., Jr. and F.P. Bretherton, 1982, Cloud cover from high-resolution scanner data: detecting and allowing for partially filled fields of view, Journal of Geophysical Research, 87:4917-4932.
- Coakley, J. A. Jr., R. D. Cess and F. B. Yurevich, 1983: The effect of tropospheric aerosol on the earth's radiation budget: a parameterization for climate models. J. Atmos. Science, 40, 116-138.

- Coakley, J. A. Jr., R. L. Bernstein and P. A. Durkee, 1987: Effect of ship stack effluents on cloud reflectivity. Science, 237, 1020-1022.
- Cooper, D.I. and G. Asrar, 1989, Evaluating atmospheric correction models for retrieving surface temperatures from the AVHRR over a tallgrass prairie, Remote Sensing of Environment, 27:93-102.
- Cracknell, A.P., 1993, A method for the Correction of Sea Surface Temperatures derived from satellite thermal infrared data in an area of Sunlint, Int. J. Remote Sensing, 14:3-8.
- Croft, T.A., 1978, Nighttime Images of the Earth from Space, Scientific American, July, pp.86-98.
- Crutzen, P. J. and M. O. Andreae, 1990: Biomass burning in the tropics: impact on atmospheric chemistry and biogeochemical cycles. Science, 250, 1669-1678.
- Crutzen, P.J., A. C. Delany, J. Greenburg, P. Haagensen, L. Heidt, R. Lueb, W. Pollock, W. Seilor, A. Wartburg, and P. Zimmerman, 1985: Tropospheric chemical composition measurements in Brazil during the dry season. J. of Atmos. Chemistry, 2, 233-256.
- Dousset, Benedicte, Pierre Flament and Robert Bernstein, 1993, Los Angeles Fires Seen from Space, EOS Transactions, American Geophysical Union, 74(3):33-38.
- Dowty, P., 1993, A Theoretical Investigation of Fire Detection with AVHRR Data, M.S. Thesis, Department of Environmental Sciences, University of Virginia, Charlottesville, Virginia, pp.89.
- Dozier, J., 1981, A method for satellite identification of surface temperature fields of subpixel resolution, Remote Sensing of Environment, 11:221-229.
- Fishman, J., P. Minnis and H.G. Reichle Jr., 1986, Use of satellite data to study tropospheric ozone in the tropics, Journal of Geophysical Research, 91: 14451-14465.
- Flannigan, Michael D., 1985, Forest Fire Monitoring Using the NOAA Satellite Series, M.S. Thesis, Department of Atmospheric Sciences, Colorado State University, Fort Collins, Colorado, 59pp.
- Flannigan, M.D. and T.H. Vonder Haar, 1986, Forest fire monitoring using NOAA satellite AVHRR, Canadian Journal of Forest Research, 16:975-982.
- Franca, J.R.A., J.M. Brustet and J. Fontan, 1993a, A multispectral remote sensing of biomass burning in West Africa, submitted to Journal of Atmospheric Chemistry.

- Franca, J-R, J-M Brustet, J. Fontan, J-M Gregoire and J.P. Malingreau, 1993b, A Multi-Spectral Remote Sensing of Biomass Burning in West Africa During 90/91 Dry Season, Presented at the XVM-EGS General Assembly, May 1993, Wiesbaden, Germany.
- Giglio, L., J. D. Kendall and C. O. Justice, 1998, Evaluation of global fire detection algorithms using simulated AVHRR infrared data, Int. J. Remote Sens., in press.
- Greenburg, J. P., P. R. Zimmerman, L. Heidt and W. Pollock, 1984: Hydrocarbon and carbon monoxide emissions from biomass burning in Brazil. J. Geophysical Res., 89, 1350-1354.
- Hallett, J., J. G. Hudson and C.F. Rogers, 1989: Characterization of combustion aerosols for haze and cloud formation. Aerosol Sci. and Tech., 10, 70-83.
- Hudson, J.G., 1991: Observations of anthropogenic cloud nuclei. Atmos. Env., 25A, 2449-2455.
- Justice C.O., J.D.Kendall, P.R.Dowty and R.J.Scholes, 1996. Satellite remote sensing of fires during the SAFARI campaign using NOAA advanced very high radiometer data, J. Geophys. Research (in press)
- Kaufman, Y.J. and T. Nakajima, 1993: Effect of Amazon smoke on cloud microphysics and albedo-analysis from satellite imagery. J. Applied Meteorology, 32, 729-744.
- Kaufman, Y.J., A. Setzer, C. Justice, C.J. Tucker, M.C. Pereira and I. Fung, 1990a, Remote Sensing of Biomass Burning in the Tropics, In: Fire in the Tropical Biota: Ecosystem Processes and Global challenges, J.G. Goldammer (ed.), Springer-Verlag, Berlin, pp371-399.
- Kaufman, Yoram J., Compton J. Tucker and Inez Fung, 1990b, Remote Sensing of Biomass Burning in the Tropics, Journal of Geophysical Research, 95(D7):9927-9939.
- Kaufman, Y.J., R.S. Fraser and R.L. Mahoney, 1991: Fossil fuel and biomass burning effect on climate-heating or cooling? Journal of Climate, 4, 578-588.
- Kaufman, Y. J., A. Setzer, D. Ward, D. Tanre, B. N. Holben, P. Menzel, M. C. Pereira and R. Rasmussen, 1992: Biomass Burning Airborne and Spaceborne Experiment in the Amazonas (BASE-A). J. Geophysical Res., 97, 14581-14599.
- Kennedy, P.J., 1992, Biomass burning studies: the use of remote sensing, Ecological Bulletins, 42:133-148.
- Kidwell, K B., 1991, NOAA Polar Orbiter Data (TIROS-N, NOAA-6, NOAA-7, NOAA-8, NOAA-9, NOAA-10, NOAA-11 & NOAA-12) Users Guide, NOAA, Washington, D.C.

- Langaas, S., 1992, Temporal and spatial distribution of savanna fires in Senegal and The Gambia, West Africa, 1989-1990, derived from multi-temporal AVHRR night images, Int. J. Wildland Fire, 2:21-36.
- Langaas, S and K Muirhead, 1988, "Monitoring" bushfires in West Africa by weather satellites, Presented at the 22nd International Symposium on Remote Sensing of Environment, October 20-26, Abidjan, Cote d'Ivoire.
- Leaitch, W.R., G.A. Isaac, J.W. Strapp, C.M. Banic and H.A. Wiebe, 1992: The relationship between cloud droplet number concentrations and anthropogenic pollution: observations and climatic implications. J. Geophysical Res., 97, 2463-2474.
- Lee, T. F. and P. M. Tag, 1990, Improved Detection of Hotspots using the AVHRR 3.7- $\mu$ m Channel, Bulletin of the American Meteorological Society, 71(12):1722-1730.
- Levine, J. S., 1991: Global biomass burning: atmospheric, climatic, and biospheric implications. In: Global Biomass Burning, J. S. Levine (Ed.). Cambridge, MA: The MIT Press.
- Malingreau, J.P., 1990, The contribution of remote sensing to the global monitoring of fires in tropical and subtropical ecosystems, In: Goldammer, J.G. (ed.), Fires in tropical biota, Ecol. Studies 82, Springer, Berlin, pp.337-370.
- Matson, M. and J. Dozier, 1981, Identification of subresolution high temperature sources using a thermal IR sensor, Photo. Engr. and Remote Sensing, 47(9):1311-1318.
- Matson, Michael and Brent Holben, 1987, Satellite detection of tropical burning in Brazil, Int. J. Remote Sensing, 8(3):509-516.
- Matson, Michael, Stanley R. Schneider, Billie Aldridge and Barry Satchwell, 1984, Fire Detection Using the NOAA-Series Satellites, NOAA Technical Report NESDIS 7, 34pp.
- Matson, Michael, George Stephens and Jennifer Robinson, 1987, Fire detection using data from the NOAA-N satellites, Int. J. Remote Sensing, 8(7):961-970.
- McClain, E. Paul, William G. Pichel and Charles C. Walton, 1985, Comparative Performance of AVHRR-Based Multichannel Sea Surface Temperatures, Journal of Geophysical Research, 90(C6):11587-11601.
- Menzel, W. P., E. C. Cutrim and E. M. Prins, 1991, Geostationary satellite estimation of biomass burning in Amazonia during BASE-A, In: Global Biomass Burning, p. 41-46, J. S. Levine (Ed.), Cambridge, MA, The MIT Press.

- Molion, L.C.B., 1991, Amazonia: burning and global climate impacts, In: Global Biomass Burning, p. 457-462, J.S. Levine (Ed.). Cambridge, MA, The MIT Press.
- Montgomery, H. and D. Endres, 1985, VAS instrument description, In: VAS Demonstration: (VISSR Atmospheric Sounder) Description and Final Report, pp. 3-8, H.E. Montgomery and L.W. Uccellini (Eds.). NASA Reference Publication 1151.
- Muirhead, K. and A.P. Cracknell, 1984, Identification of gas flares in the North Sea using satellite data, Int. J. Remote Sensing, 5(1):199-212.
- Muirhead, K. and A.P. Cracknell, 1985, Straw burning over Great Britain detected by AVHRR, Int. J. Remote Sensing, 6(5):827-833.
- Nath, A. Narendra, M.V. Rao and K.H. Rao, 1993, Observed high temperatures in the sunglint area over the ocean. International Journal of Remote Sensing, 14(5):849-853.
- Penner, J. E., R. E. Dickenson, C. A. O'Neill, 1992: Effects of aerosol from biomass burning on the global radiation budget. Science, 256, 1432-1434.
- Pereira, M.C. and A.W. Setzer, 1993, Spectral characteristics of deforestation fires in NOAA/AVHRR images, Int. J. Remote Sensing, 14(3):583-597.
- Pereira, Alfredo C., Jr., Alberto W. Setzer and Joao R. dos Santos, 1991, Fire Estimates in Savannas of Central Brazil with Thermal AVHRR/NOAA Calibrated by TM/Landsat, Presented at the 24th International Symposium on Remote Sensing of Environment, Rio de Janeiro, Brazil, 27-31 May 1991.
- Prins, E. M., 1989, Geostationary satellite detection of biomass burning in South America, MS thesis, University of Wisconsin-Madison, 141 pp.
- Prins, E. M. and W.P. Menzel, 1992, Geostationary satellite detection of biomass burning in South America, Int. J. Remote Sensing, 13:2783-2799.
- Prins, E. M. and W.P. Menzel, 1993, Application of the GOES VAS Automated Biomass Burning Algorithm (ABBA) in South America: A trend analysis from 1983-1991, to be submitted.
- Radke, L. F., J. H. Lyons, P. V. Hobbs, D. A. Hegg, D. V. Sandberg and D. E. Ward, 1990: Airborne monitoring and smoke characterization of prescribed fires on forest lands in western Washington and Oregon. Gen. Tech. Rep. PNW-GTR-251, Portland, OR: U.S.D.A., Forest Service, Pacific Northwest Research Station.
- Riggan P.J., J.A. Brass and R.N. Lockwood, 1993, Assessing Fire Emissions from Tropical Savanna and Forests of Central Brazil, Photogram Engineering and Remote Sensing, (in press)

- Robinson, J M., 1991a, Fire from space: Global fire evaluation using infrared remote sensing, Int. J. Remote Sens., 12(1):3-24.
- Robinson, J M., 1991b, Problems in global fire evaluation: Is remote sensing the solution?, In: Global Biomass Burning, MIT Press, Joel S. Levine (ed.), Cambridge, USA, pp.67-73.
- Rogers, C.F., J.G. Hudson, B. Zielinska, R.L. Tanner, J. Hallett and J.G. Watson, 1991: Cloud condensation nuclei from biomass burning. In: Global Biomass Burning, p. 431-438,
- Roy, D., L. Giglio, J. D. Kendall, and C. O. Justice, 1998, Multitemporal active-fire based burn scar detection algorithm, Int. J. Remote Sens. Lett., in press.
- Scholes R.J., D Ward and C.O. Justice, 1996, Emissions of trace gases and aerosol particles due to biomass burning in southern hemisphere Africa - J. Geophys. Research (in press).
- Schwalb, Arthur, 1982, Modified Version of the TIROS-N/NOAA A-G Satellite Series (NOAA E-J)-Advanced TIROS-N (ATN), NOAA Technical Memorandum NESS 116, NOAA, Washington, D.C.
- Shea R.W., B.W. Shea, J.B.Kauffman, D.E. Ward, C.J.Haskins and M.C. Scholes, 1996. Fuel biomass and combustion factors associated with fires in savanna ecosystems of South Africa and Zambia, J. Geophys. Research (in press).
- Setzer, Alberto W. and Marcos C. Pereira, 1991a, Operational Detection of Fires in Brazil with NOAA-AVHRR, Presented at the 24th International Symposium on Remote Sensing of Environment, Rio de Janeiro, Brazil, 27-31 May 1991.
- Setzer, Alberto W. and Marcos C. Pereira, 1991b, Amazonia Biomass Burnings in 1987 and an Estimate of Their Tropospheric Emissions, Ambio, 20(1):19-22.
- Stephens, G. and M. Matson, 1989, Fire Detection Using the NOAA-N Satellites, Presented at the 10th Conference on Fire and Forest Meteorology, April 17-21, Ottawa, Canada.
- Stith, J.L., L.F. Radke and P.V. Hobbs, 1981: Particle emissions and the production of ozone and nitrogen oxides from the burning of forest slash. Atmospheric Environment, 15, 73
- Sullivan, III, W.T., 1989, A 10 km Resolution Image of the Entire Night-time Earth Based on Cloud-free Satellite Photographs in the 400-1100 nm Band, Int. J. Remote Sensing, 10(1):1-5.

Twomey, S.A.,1977: The influence of pollution on the short wave albedo of clouds. J. Atmos.Sci., **34**, 1149-1152.

Twomey, S. A., M. Piepgrass and T. L. Wolfe, 1984: An assessment of the impact of pollution on the global cloud albedo. Tellus, **36b**, 356-366.

Twomey, S.A., 1991: Aerosols, clouds, and radiation. Atmos. Env., **25A**, 2435-2442.

Ward, D.E., R. Susott, J. Kauffman, R. Babbitt, B. N. Holben, Y.J. Kaufman, A. Setzer, R. Rasmussen, D. Cumming and B. Dias, 1992: Emissions and burning characteristics of biomass fires for cerrado and tropical forest regions of Brazil - BASE-B experiment', J. Geophys. Res., **97**, 14601-14619.

## APPENDIX 1. Previous ATBD Reviews

The 1993 ATBD was reviewed by letter and by panel, the reviewer comments were addressed in an updated version of the ATBD (Feb 1994).

As part of the SWAMP LAND review in May 1996 the ATBD was reviewed again. The comments from the SWAMP reviewers and the authors reply (*italicized text*) are attached as this Appendix.

### SWAMP Land Review May 1996

#### Section 6.2.5a. Data Product: MOD14 - Thermal anomalies (fire, size, temp)

(Review based on ATBD-MOD-15, Version 1.2.2, dated Feb. 21, 1994, and presentation at workshop, May 16, 1996)

##### (a) technical/scientific soundness of the algorithm/approach described

(Rating: 9/3)

The primary goals of this algorithm are to automatically identify the physical location of fires and characterize the frequency of occurrence, strength, total emitted energy, and smoldering/flaming ratio within a given pixel. The full set of fire characteristics requires that the fires exceed a certain minimum area test, which results in a detectable temperature threshold to be exceeded. The basis for the basic detection and first order characterization of fire-containing pixels is sound. The algorithms have heritage from systematic analysis of GOES VAS sensor data (ABBA algorithm), and from analysis of AVHRR data. The algorithms for fire detection and location are relatively simple, consisting of temperature and/or reflectance thresholds of a few select bands from the MODIS suite. The apparent temperatures are corrected for gaseous absorption using precipitable water vapor derived from other MODIS bands and climatological lookup tables. The latter have the greatest potential for error in the algorithms, and will need to be carefully implemented. More detailed analysis of the fires requires characterization of the background temperatures against which the fire is detected. This uses a spatial analysis algorithm typically involving a 10x10 suite of adjacent pixels. The characteristics of fire-containing pixels that meet a final set of logical conditions tested against this background are then saved. The algorithms depends to some extent on cloud screen approaches and temperature calibrations which are to be accommodated by other groups within the MODIS team. (Rating: 9)

The more thorough characterization of the fire properties follows the identification of fire-containing pixels. These algorithms are not as well defined and are currently based on theoretical considerations without a detailed assessment of accuracy through applications. In the theoretical analyses, the relationship between total emitted energy and  $DT^4$  for low values under-predicts the emitted energy by factors of 3-5. The errors are less for higher values of  $DT^4$ .



- We performed detailed sensitivity studies of heterogeneous fire pixels and found a new expression that fits both small and large fires. Application to 40 m resolution MAS DATA from SCAR-B show that the energy expression is very sensitive to the subpixel fire size and fire temperature. We also checked the model predictions against MAS data for the dependence of the apparent temperature to the thermal energy in several wavelengths, and found a very good agreement.

The determination of the smoldering/flaming ratio is very model dependent and the value of this product is not apparent as presented in this document. Will the level of uncertainty preclude its use in an effective way? The determination of fire size and temperature, stated to not be implemented at this stage, also carries a large degree of uncertainty.

- Fire size and temperature are very sensitive to the representation of the background temperature, mainly at 11 microns. Sensitivity studies show that it cannot be done on a 1 km resolution, and therefore we do not plan to produce fire temperature and size -- only energy and smoldering/flaming ratio.

The new results on the estimate of flame/smoldering ratio presented at the algorithm review did not appear to resolve the ambiguity in determining this ratio accurately. Perhaps the most compelling reason to reduce the effort on the flame/smolder ratio is that the AM platform only has one observation each day, in the morning. Fires are most prevalent in the afternoon, and to know the true gas emission from a fire, the time history of flame and smoldering is required.

- Agree.

There is a high level of non-uniqueness in this calculation, and therefore the value to the land science community is unclear. The fire problem corresponds to a very large signal corrupted by very large "noise", where the noise means effects of smoke and clouds,

- There is no effect of smoke at 4 and 11  $\mu\text{m}$  -- the particles are too small to have an impact. Subpixel clouds will have a very small effect on the energy and some effect on the smoldering/flaming ratio.

the fact that there are not simply two fire temperatures (1000 and 600 K), temporal variability, etc. The result may be better thought of as an indicator rather than a real solution for the fire situation in the 1 km pixels. (Rating: 3)

- Fire thermal energy is a strong parameter. Sensitivity studies and the new SCAR-B results show its robustness and independence of resolution in the 40 m-1 km range. It is the most significant quantitative parameter that we will be deriving from MODIS. The number of fires has only a relative meaning.

**(b) value of the data product to the Land science community (Rating: 6)**

- *Fire is not only a land product but it is a multidisciplinary MODIS product with value to the atmospheric community.*

The products will be very valuable to several aspects of the land science community. Global modeling of climate and atmosphere dynamics will be able to capitalize on estimates of fire frequency and gaseous emissions. Fire also affects land albedo, nutrient type and amount, erosion potential, and hydrological budgets. Finally, fires are a key part of many ecosystem disturbance models and have many indirect and direct effects on ecosystem structure and evolution. Nevertheless, a list of end-users of these data products has not been explicitly defined.

- *Listing end users explicitly is not our intention -- there are several PI's from the modelling community that have shown an interest in fire data. An early expression of these needs was raised at the IGBP-DIS data requirements in Toulouse 1992 when IGAC and GCTE made a strong case for fire data products. A similar response was seen at the last Chapman conference on fire and the October 1996 and March 1998 IGBP-DIS Fire Algorithm Group meetings.*

However, the usefulness will be adversely affected by the non-trivial problem of overpass at a fixed time and the diurnal behaviour of fires - thus a large potential for bias in the satellite-derived products.

- *We shall be combining MODIS, geostationary satellite, ASTER, and LANDSAT data to provide an overall fire monitoring system.*

**(c) soundness of the validation strategy (Rating: 5)**

Calibration of the temperature estimates from MODIS are important, and the ATBD raises the issues of the calibration for the fire channel as a potential problem (T<sup>4</sup>). Post-launch calibration will only be possible through vicarious methods. Validation will include the use of higher resolution sensors (e.g. MODIS Airborne Simulator (MAS)), as well as participation in pre-launch campaigns. Post-launch validation will include the use of GOES and METEOSAT data.

- *GOES and METEOSTAT will not be used for calibration rather for qualitative validation of fire distribution and for supplementing the diurnal cycle.*

THE MOON IS AROUND 400K AND MAY BE USED FOR CALIBRATION ??

Though of much lower spatial resolution, these sensors provide much greater temporal frequency. Overall, the validation strategy is not well defined. These algorithms will require both continued validation of the strategy through simulations in the laboratory and the analysis of actual data from AVHRR, GOES, and/or MAS. There is some concern that the methods on which these algorithms are based include significant interactive input and the use of plume analysis. Also, there are not yet any test examples of the algorithm in operation.

- WE ARE CLOSE IN A FEW WEEKS WE SHALL HAVE OVER 10,000 MAS OBSERVED FIRES FROM BRAZIL TO ANALYZE

A significant opportunity exists to use ASTER data in post-launch validation and verification studies. This opportunity was not identified in the ATBD nor the workshop presentation. Though ASTER does not have the radiometric resolution to determine fire and smoldering temperatures, the spatial resolution coupled with the available thermal measurements could assist area calculation studies significantly.

- *We intend to use ASTER to help with burn scar and fire occurrence validation.*

**(d) extent to which 1994 ATBD review issues have been addressed (N/A)**

Not reviewed at the 1994 ATBD review.

- *The ATBD was reviewed by letter and panel in 1994.*

**(e) near-term recommendations for improvements to the data product**

the end products, in particular the products of Step 9 in the algorithm, need to be better defined for a range of conditions.

the algorithm should be field tested and/or validated on some test data.

- *Definitely.*

**(f) long-term recommendations for improvements or additions to the data product**

flow-through testing of the algorithm should be conducted.

- *Data flow-through is being tested as part of the land V1 and V2 deliveries - fires are included in the modis simulation data set and are identified by the algorithm. In addition, errors are being built into the simulation data set to test the robustness of the code.*

**6.2.5b. Balance of Land Data Products as generated by EOS-AM 1 (i.e. ASTER, MISR, MODIS) to meet the needs of the broader Land science community**

**(a) extent to which the data product (and its accuracies) is useful to the broader land science community and meshes with the other instrument data products (Rating: 9)**

The fire product is a unique and important contribution to the land science community. The products could have impact on a number of different areas, including atmospheric modeling, hydrology, and ecosystem dynamics. As yet, there are no global inventories of fire occurrence, frequency, and magnitude, and this will fill an important gap in our knowledge of land dynamics. However, there are still issues regarding the accuracy of the derived fire information (e.g. size, smoldering/flame ratio etc.), and a well-defined customer base is not identified.

**(b) assessment of plans for the comparison or enhancement of similar data products from the other instruments? (Rating: 0)**

There are no plans for comparison or enhancement of similar data products from other instruments.

**(c) recommendations for changes to improve the balance of land data products.**

None.

---

**6.2.6a. Data Product: MOD40 Thermal anomalies (Gridded version)**

(Review based on ATBD-MOD-15, Version 1.2.2, dated Feb. 21, 1994, and presentation at workshop, May 16, 1996)

**(a) technical/scientific soundness of the algorithm/approach described**

(Rating: 9)

The data products will ultimately be reduced to gridded composites. These composites include 10x10 km and 0.5°x 0.5° ( 50x50 km) grid cells composited to daily, 10 day, and monthly temporal levels. The main information contained in the grid cells (fire location, temperature and reflectance quantities used to identify the fire) will be essential and valuable information for assessing overall quality of the product and for possible reprocessing as experience is gained with the algorithm. The derived data products (e.g. total emitted energy) is of less apparent value at this stage, but may be important once validation studies have been performed.

**(b) value of the data product to the Land science community (Rating: 9)**

These will be new and important information for the land science community. The atmospheric science community will also benefit from these products.

**(c) soundness of the validation strategy (Rating: 5)**

It is unclear from the ATBD what level of information exists on the temporal frequency of fires as detected remotely, and the utility of gridded products in these analysis. Thus the validation strategy will be critical. The issues raised in the review of the algorithm apply here.

**(d) extent to which 1994 ATBD review issues have been addressed (N/A)**

Not reviewed at the 1994 ATBD review

**(e) near-term recommendations for improvements to the data product**

None.

**(f) long-term recommendations for improvements or additions to the data product**

None.

**6.2.6b. Balance of Land Data Products as generated by EOS-AM 1 (i.e. ASTER, MISR, MODIS) to meet the needs of the broader Land science community**

**(a) extent to which the data product (and its accuracies) is useful to the broader land science community and meshes with the other instrument data products (Rating: 9)**

This is a somewhat unique product relative to the main activities of the broader land science community. Nevertheless, there has been less experience in the use of such data, and it is likely to play an important role in many levels of scientific analysis and environmental monitoring. In fact, the gridded product will likely have great impact because of the clear signature of human activity behind many of the fires.

**(b) assessment of plans for the comparison or enhancement of similar data products from the other instruments? (Rating: 0)**

None listed.

- *We will be comparing modis data to those from the AVHRR's and the geostationary systems.*

**(c) recommendations for changes to improve the balance of land data products**  
None.